

Optimal navigation in two-dimensional flows: control theory and reinforcement learning

Vladimir Parfenyev*

*Landau Institute for Theoretical Physics, Russian Academy of Sciences,
1-A Akademika Semenova av., 142432 Chernogolovka, Russia and
HSE University, Faculty of Physics, Myasnitskaya 20, 101000 Moscow, Russia*
(Dated: December 29, 2025)

Zermelo’s navigation problem seeks the trajectory of minimal travel time between two points in a fluid flow. We address this problem for an agent – such as a micro-robot or active particle – that is advected by a two-dimensional flow, self-propels at a fixed speed smaller than or comparable to the characteristic flow velocity, and can steer its direction. The flows considered span increasing levels of complexity, from steady solid-body rotation to the Taylor-Green flow and fully developed turbulence in the inverse cascade regime. Although optimal control theory provides time-minimizing trajectories, these solutions become unstable in chaotic regimes realized for complex background flows. To design robust navigation strategies under such conditions, we apply reinforcement learning. Both action-value (Q-learning) and policy-gradient (one-step actor-critic) methods achieve successful navigation with comparable performance. Crucially, we show that agents trained on coarse-grained turbulent flows – retaining only large-scale features – generalize effectively to the full velocity field. This robustness to incomplete flow information is essential for practical navigation in real-world oceanic and atmospheric environments.

I. INTRODUCTION

The quest for the optimal path between two points, a cornerstone of navigation and control theory, finds profound expression in the classical Zermelo’s navigation problem. Originally formulated by Ernst Zermelo in his seminal work [1], the problem seeks the trajectory of minimal travel time for an agent moving with constant self-propulsion speed in a known fluid flow by adjusting the steering direction. Beyond its theoretical elegance, this framework holds critical importance for a variety of modern applications, from micro-robots navigating vascular networks for targeted drug delivery [2–4], to autonomous underwater and aerial vehicles operating in oceanic and atmospheric environments [5–8]. The core challenge lies in the interplay between the agent’s own propulsion and the advective power of the flow, which often dominates the dynamics, necessitating a control strategy that can exploit environmental forces rather than simply resist them.

The study of Zermelo’s problem has traditionally been approached through the lens of optimal control theory. Within this framework, one can derive a differential equation governing the evolution of the agent’s steering direction, which serves as the necessary condition for optimality (see, e.g., Ref. [9, Sec. 2.7]). For relatively simple flow fields, this equation admits analytical solutions [10], enabling the construction of optimal trajectories. In more complex environments, however, numerical techniques are required. The challenge is further complicated by the absence of a known initial condition for the steering equation, which in practice must be determined using shooting methods [11].

This classical formulation faces two crucial limitations. First, calculating the optimal path requires perfect and global knowledge of the flow field. Second, the resulting optimal trajectories can be unstable. In systems exhibiting chaotic dynamics – characterized by exponential separation of nearby trajectories – infinitesimal uncertainties in initial conditions or control inputs are amplified, leading to drastic deviations from the planned route [12, 13]. In these cases, pre-computed optimal control strategies become ineffective. Both limitations are violated in turbulent flows, which dominate oceanic and atmospheric environments [14, 15]. The requirement for perfect flow knowledge is unrealistic, as operational forecasts are inherently coarse-grained, forcing an agent to operate with incomplete information. Furthermore, turbulence is a canonical example of a chaotic system, meaning the stability condition is violated.

In response to these challenges, the field has explored alternative paradigms, including heuristic [16–18] and data-driven methods [13, 19–26]. The rise of machine learning has opened new avenues, with reinforcement learning (RL) emerging as a particularly powerful model-free framework for complex control [27]. The RL formulation treats navigation as a sequential decision-making process in which an agent learns a policy – a mapping from states (e.g., positions) to actions (e.g., heading adjustments) – by maximizing a cumulative reward, typically defined in terms of minimizing travel time to a target. Early studies have highlighted the promise of this approach. For instance, the work of Colabrese et al. [20] demonstrated that smart active particles could use Q-learning to navigate vortex flows, effectively discovering physical strategies like surfing on specific flow structures. Similarly, Biferale et al. [13] explored the use of RL to solve Zermelo’s problem in synthetic two-dimensional turbulent flows, showing that agents can learn to lever-

* parfenius@gmail.com

age flow structures to minimize travel time. However, a systematic investigation across a hierarchy of flows from regular to fully turbulent, and crucially, an assessment of the robustness and generalization capabilities of learned policies under realistic information constraints, remains an open area of research.

This work directly addresses this gap by presenting a comprehensive study of optimal navigation across a spectrum of two-dimensional flows. We examine environments of increasing complexity, from steady solid-body rotation to the advection by Taylor-Green vortices and, finally, to turbulent flows in the inverse cascade regime. The focus on two-dimensional flows is motivated by both computational tractability and their relevance to large-scale atmospheric and oceanic currents [14, 15]. Our analysis first confirms that while optimal control theory yields nominal time-minimizing trajectories, its practical utility is significantly reduced in chaotic regimes due to the instability discussed above. To develop more robust strategies, we then turn to RL and examine two algorithmic classes: an action-value approach based on Q-learning and a policy-gradient approach, implemented as a one-step actor-critic algorithm [27]. We compare the resulting RL-derived trajectories with those obtained through classical optimal control to assess the capabilities of RL algorithms. The central and most significant finding of our study is that RL agents trained not on a full turbulent field, but on a coarse-grained version retaining only large-scale flow features, demonstrate remarkable generalization by successfully navigating within the fully resolved turbulent environment. This ability to operate effectively with incomplete, low-resolution information is not only of theoretical interest but also a critical step toward the practical deployment of autonomous systems in real-world oceanic and atmospheric settings.

By maintaining a detailed presentation, our work serves a dual purpose: advancing the research frontier and providing a valuable reference for educational purposes. The code that supports the findings of this study are openly available in Ref. [28]. The remainder of this paper is organized as follows. In Section II, we formulate the Zermelo’s problem and introduce the equations of motion for the agent. Section III describe the hierarchy of flows we study. Section IV details the application of optimal control theory and analyzes the stability of the resulting trajectories. Section V explains our reinforcement learning framework and discusses its application to the presented examples. Section VI is devoted to navigation in turbulent environment with incomplete flow information. Finally, Section VII summarizes our findings.

II. PROBLEM SETUP

We study the motion of an agent navigating a two-dimensional flow field $\mathbf{v}(\mathbf{r}, t)$, which is governed by the

kinematic equation

$$\frac{d\mathbf{R}_t}{dt} = \mathbf{v}(\mathbf{R}_t, t) + V_0 \begin{pmatrix} \cos \theta_t \\ \sin \theta_t \end{pmatrix}, \quad (1)$$

where $\mathbf{R}_t = (X_t, Y_t)$ is the position of the agent at time t in Cartesian coordinates. The dynamics combines passive advection by the background flow $\mathbf{v}(\mathbf{R}_t, t)$, which represents the external environmental velocity such as oceanic or atmospheric currents, and active self-propulsion at constant speed V_0 . The steering direction θ_t serves as the control variable that the agent can adjust in real-time. The objective of Zermelo’s problem [1] is to find a control policy $\theta_t = \theta(\mathbf{R}_t, t)$ that minimizes the total travel time T for a journey between two predefined points \mathbf{r}_A and \mathbf{r}_B . This challenge originated in the context of airship flight [29] and remains a canonical problem in optimal control theory.

The nature of the solution is dependent on the relative strength of the flow. In the regime, where the agent’s speed V_0 significantly exceeds the characteristic flow velocity, one may expect that a trivial strategy of continuously orienting the propulsion vector directly toward the target \mathbf{r}_B is close to optimal. The problem becomes more challenging in the opposing regime, where the flow exerts a strong influence. Under these conditions, the agent must strategically ride the current, often making counter-intuitive moves away from the target to exploit favorable flow structures for an overall reduction in travel time. This latter complex regime is the primary focus of our work.

III. BACKGROUND FLOWS

This section introduces the hierarchy of background flows considered in our study. The first two examples are adopted from Ref. [10], and for them the Zermelo’s problem admits a semi-analytical solution. We then move on to more complex flows designed to test the performance of our methods in increasingly challenging environments.

A. Steady vortex flow

In the first example, the background velocity field corresponds to steady solid-body rotation and it is given by

$$\mathbf{v}(x, y) = (-\omega y, \omega x)^T. \quad (2)$$

The starting point is $(x_A, y_A) = (1/2, \sqrt{3}/2)$ and our aim is to reach the end point $(x_B, y_B) = (1, 0)$ in the shortest time. The agent’s speed $V_0 = 1$, and we set $\omega = 0.9$. Note that traveling upstream along a streamline is not an optimal solution.

B. Steady sink and time-varying vortex flow

In the second example, we consider a divergent and time-varying flow. The background velocity is given by

$$\mathbf{v}(x, y, t) = \begin{pmatrix} -0.3x - (0.5 - t)y \\ -0.3y + (0.5 - t)x \end{pmatrix}. \quad (3)$$

The flow model represents a constant sink plus a vortex that linearly changes vorticity with time. The goal is to start from the point $(x_A, y_A) = (1/2, \sqrt{3}/2)$ and reach the point $(x_B, y_B) = (1, 0)$ in the shortest time. The agent's speed is $V_0 = 1$. The main purpose of this example is to demonstrate the applicability of the discussed approaches to time-varying and divergent flows.

C. Taylor-Green vortices

In the third example, the background velocity is incompressible, $\text{div } \mathbf{v} = 0$, and it is given by

$$\mathbf{v}(x, y) = \begin{pmatrix} u_0 \sin(kx) \cos(ky) \\ -u_0 \cos(kx) \sin(ky) \end{pmatrix}. \quad (4)$$

The corresponding vorticity is $\varpi = \partial_x v_y - \partial_y v_x = 2u_0 k \sin(kx) \sin(ky)$. Thus, the velocity field looks like a checkerboard of counter-rotating vortices. A similar velocity field can be generated on the fluid surface due to the nonlinear interaction of two orthogonal standing waves [30–35].

We assume that the motion is confined in space within $[0, L]^2$ domain, where $L = 2\pi$. We set $u_0 = 1$, $k = 3$, and the agent's speed is $V_0 = 0.1$. The starting point is $(x_A, y_A) = (2\pi/3, \pi/3)$ and the end point is $(x_B, y_B) = (3\pi/2, 3\pi/2)$. The main challenge in this example is to escape vortex traps along the way.

D. 2D Turbulence

Finally, we consider a two-dimensional turbulent flow, which is generated by numerically solving the incompressible forced 2D Navier-Stokes equations for a fluid of unit density

$$\partial_t \mathbf{v} + (\mathbf{v} \cdot \nabla) \mathbf{v} = -\nabla p + \nu \nabla^2 \mathbf{v} - \alpha \mathbf{v} + \mathbf{f}, \quad \nabla \cdot \mathbf{v} = 0, \quad (5)$$

where \mathbf{v} is 2D velocity, p is the pressure, $\nu = 5 \cdot 10^{-3}$ is the kinematic viscosity, $\alpha = 0.2$ is the linear bottom drag, and \mathbf{f} is an external random forcing. The equations are solved in a doubly periodic square domain of size $L = 2\pi$. The forcing \mathbf{f} is isotropic in space and shortly correlated in time, with a Gaussian spatial spectrum centered at wavenumber $k_f = 5.5$ and having a standard deviation $\delta_f = 1.0$. The energy injection rate $\epsilon = \langle \mathbf{v} \cdot \mathbf{f} \rangle$ is an externally controlled parameter set to $\epsilon = 10$.

DNS results are obtained by integrating (5) using the GeophysicalFlows.jl pseudospectral code [36], fully dealiased by the two-thirds rule. We use a 512^2 grid with a

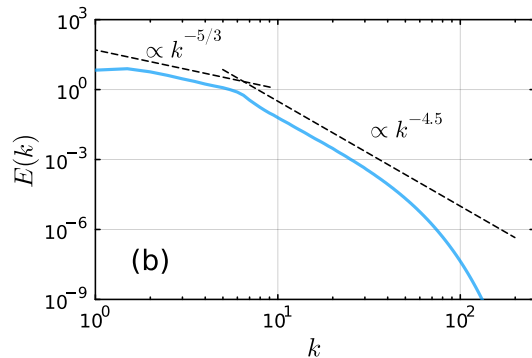


FIG. 1. Energy spectrum for DNS of 2d turbulence.

fixed integration time step $dt = 2 \cdot 10^{-4}$, resulting in a Courant number < 0.3 . The forcing correlation time is also dt . Starting from rest, the simulation is run until it reaches a non-equilibrium stationary state, observed by the saturation of the total kinetic energy. Snapshots of the velocity field are then output at an interval of $\tau = 5 \cdot 10^{-3}$ over a total duration of $T_{tot} = 6.15$, yielding 1230 snapshots for analysis.

The resulting flow is characterized by dimensionless numbers $Re = UL/\nu \approx 8 \cdot 10^3$ and $Rh = U/(\alpha L) \approx 5$, where $U \approx 6.3$ is the root-mean-square velocity. The mean energy spectrum, shown in Fig. 1, confirms the established phenomenology of forced 2D turbulence. In the inverse energy cascade range $k < k_f$, the spectrum follows the theoretical $E(k) \propto k^{-5/3}$ scaling [15], while in the direct enstrophy cascade range $k > k_f$, the bottom drag leads to a steeper slope than the classical $E(k) \propto k^{-3}$ prediction [37].

To evaluate our navigation algorithms, we employ both instantaneous snapshot and the full time-dependent flow data. The agent's self-propulsion speed is set to $V_0 \approx 4.5$, which corresponds to 30% of the maximum flow velocity. Experimentally, flows with similar statistical properties can be excited by Faraday waves on the fluid surface [38–42] or by the Lorentz force in a thin conducting fluid layer over a magnet array [43–48].

IV. OPTIMAL CONTROL THEORY

In this section, we describe how to apply control theory to determine the time-minimizing trajectories for an agent moving from point \mathbf{r}_A to point \mathbf{r}_B . First, we derive a necessary condition that the steering direction θ_t must satisfy along an optimal trajectory. Our analysis assumes only a basic familiarity with the calculus of variations and draws heavily on Ref. [9, Sec. 2.7]. For readers acquainted with Pontryagin's minimum principle, a similar result is derived in Ref. [10]. Following the derivation of the Zermelo equation, we apply it to the specific examples outlined in the previous section.

A. Zermelo's equation

The problem of finding the minimum-time trajectory and the corresponding travel time T can be addressed through variational calculus. We seek to minimize the functional $\int_0^T dt L(t, \mathbf{R}_t, \dot{\mathbf{R}}_t)$, where \mathbf{R}_t obeys the equation of motion (1) and boundary conditions $\mathbf{R}_0 = \mathbf{r}_A$ and $\mathbf{R}_T = \mathbf{r}_B$. This constitutes a constrained optimization problem that can be solved using the method of Lagrange multipliers. For the minimum-time problem, the cost function is simply $L(t, \mathbf{R}_t, \dot{\mathbf{R}}_t) \equiv 1$, yielding the extended functional

$$J = \int_0^T dt \left(1 - \lambda_X(t) \left[V_0 \cos \theta_t + v_x(t, X_t, Y_t) - \dot{X}_t \right] - \lambda_Y(t) \left[V_0 \sin \theta_t + v_y(t, X_t, Y_t) - \dot{Y}_t \right] \right). \quad (6)$$

The Lagrange multipliers $\boldsymbol{\lambda}_t = (\lambda_X(t), \lambda_Y(t))$ play a role analogous to canonical momentum in classical mechanics. Following this analogy, we introduce the Hamiltonian $H = -1 + \lambda_X(t) [V_0 \cos \theta_t + v_x(t, X_t, Y_t)] + \lambda_Y(t) [V_0 \sin \theta_t + v_y(t, X_t, Y_t)]$, and then the functional J can be compactly written as

$$J = \int_0^T dt \left(\boldsymbol{\lambda}_t \cdot \dot{\mathbf{R}}_t - H \right). \quad (7)$$

Next, the necessary conditions for an extremum are derived by setting the first variation of the functional to zero, $\delta J = 0$. However, in contrast to classical mechanics, the terminal time T is not specified, and we should take into account its differential changes:

$$\delta J = \int_0^T dt \left[-\frac{\partial H}{\partial \mathbf{R}_t} \delta \mathbf{R}_t - \frac{\partial H}{\partial \boldsymbol{\lambda}_t} \delta \boldsymbol{\lambda}_t - \frac{\partial H}{\partial \theta_t} \delta \theta_t + \dot{\mathbf{R}}_t \cdot \delta \boldsymbol{\lambda}_t + \boldsymbol{\lambda}_t \cdot \delta \dot{\mathbf{R}}_t \right] + \delta T (\boldsymbol{\lambda}_T \cdot \dot{\mathbf{R}}_T - H(T)). \quad (8)$$

The last term in the square brackets can be integrated by parts, which produces additional boundary term $\boldsymbol{\lambda}_T \cdot \delta \mathbf{R}_T$. As the position of the final point is fixed, we get $d\mathbf{R}_T = \delta \mathbf{R}_T + \dot{\mathbf{R}}_T \delta T = 0$, and therefore

$$\delta J = \int_0^T dt \left[\left(\dot{\mathbf{R}}_t - \frac{\partial H}{\partial \boldsymbol{\lambda}_t} \right) \delta \boldsymbol{\lambda}_t - \frac{\partial H}{\partial \theta_t} \delta \theta_t - \left(\frac{\partial H}{\partial \mathbf{R}_t} + \dot{\boldsymbol{\lambda}}_t \right) \delta \mathbf{R}_t \right] - H(T) \delta T. \quad (9)$$

For $\delta J = 0$ to hold for arbitrary variations $\delta \mathbf{R}_t$, $\delta \boldsymbol{\lambda}_t$, $\delta \theta_t$, and δT , their coefficients must vanish identically. This yields the following necessary conditions for the optimal path:

$$\dot{\mathbf{R}}_t = \frac{\partial H}{\partial \boldsymbol{\lambda}_t}, \quad \dot{\boldsymbol{\lambda}}_t = -\frac{\partial H}{\partial \mathbf{R}_t}, \quad \frac{\partial H}{\partial \theta_t} = 0, \quad \boldsymbol{\lambda}_T \cdot \dot{\mathbf{R}}_T = 1. \quad (10)$$

The obtained system is governed by four differential equations (for \mathbf{R}_t and $\boldsymbol{\lambda}_t$) with four boundary conditions (the fixed start and end points, $\mathbf{R}_0 = \mathbf{r}_A$ and $\mathbf{R}_T = \mathbf{r}_B$), one optimality condition for the control θ_t , and one transversality condition $\boldsymbol{\lambda}_T \cdot \dot{\mathbf{R}}_T = 1$ for the free terminal time T . The state equation $\dot{\mathbf{R}}_t = \partial H / \partial \boldsymbol{\lambda}_t$ simply restates the original equations of motion (1). From $\dot{\boldsymbol{\lambda}}_t = -\partial H / \partial \mathbf{R}_t$ and $\partial H / \partial \theta_t = 0$, we obtain

$$\dot{\lambda}_t^x = -\lambda_t^x \partial_x v_x(t, \mathbf{R}_t) - \lambda_t^y \partial_x v_y(t, \mathbf{R}_t), \quad (11)$$

$$\dot{\lambda}_t^y = -\lambda_t^x \partial_y v_x(t, \mathbf{R}_t) - \lambda_t^y \partial_y v_y(t, \mathbf{R}_t), \quad (12)$$

$$\tan \theta_t = \lambda_t^y / \lambda_t^x. \quad (13)$$

The optimal control is determined by $\theta_t = \arctan(\lambda_t^y / \lambda_t^x)$. A more useful form is the Zermelo's equation, derived by differentiating this expression with respect to time and using expressions (11) and (12):

$$\dot{\theta}_t = \partial_x v_y \sin^2 \theta_t - \partial_y v_x \cos^2 \theta_t + (\partial_x v_x - \partial_y v_y) \sin \theta_t \cos \theta_t, \quad (14)$$

where the velocity gradients are evaluated along the agent trajectory \mathbf{R}_t . This equation describes how the vehicle must continuously adjust its heading in response to the spatial gradients of the flow field to maintain a minimum-time trajectory.

The complete Two-Point Boundary Value Problem (TPBVP) is thus defined by coupling the equations of motion (1) with the heading evolution equation (14). The boundary conditions are the fixed start and end positions, $\mathbf{R}_0 = \mathbf{r}_A$ and $\mathbf{R}_T = \mathbf{r}_B$. The initial heading θ_0 is not specified, making this a free condition. The standard numerical approach to solve this TPBVP is the shooting method: an initial guess for θ_0 is iteratively refined until the resulting trajectory, obtained by forward integration of the system, satisfies the terminal condition $\mathbf{R}_T = \mathbf{r}_B$ within a desired tolerance. More details on the numerical procedure will be provided later when discussing specific examples. Note that once the initial heading θ_0 is known, the optimal path can be integrated autonomously, provided the agent can measure the local velocity field gradients, see Eq. (14).

B. Example 1: Steady vortex flow

For the background velocity field $\mathbf{v}(x, y) = (-\omega y, \omega x)^T$, the Zermelo's equation (14) has a simple solution $\theta_t = \theta_0 + \omega t$. Integrating the equations of motion (1) from the starting point $(X_0, Y_0) = (x_A, y_A)$ yields the trajectory:

$$X_t = x_A \cos(\omega t) + V_0 t \cos(\omega t) \cos \theta_0 \quad (15)$$

$$-y_A \sin(\omega t) - V_0 t \sin(\omega t) \sin \theta_0,$$

$$Y_t = y_A \cos(\omega t) + V_0 t \cos(\omega t) \sin \theta_0 \quad (16)$$

$$+x_A \sin(\omega t) + V_0 t \sin(\omega t) \cos \theta_0.$$

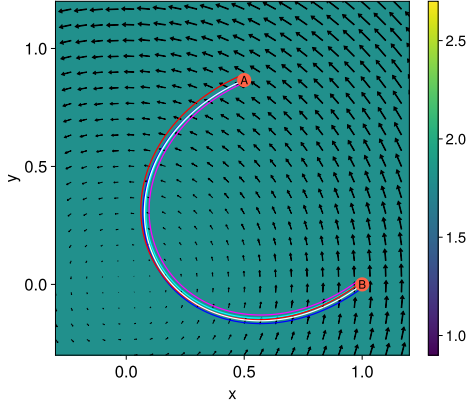


FIG. 2. Optimal control solution (white line) for the steady vortex flow, see Sections III A. Near-optimal trajectories are shown in cyan and blue for the initial control angle $\theta_0 \pm \pi/360$, and in magenta and red for the initial position error $\Delta = 0.025$ in x_A and y_A .

The initial heading θ_0 and total travel time T are determined by enforcing the terminal condition $(X_T, Y_T) = (x_B, y_B)$. For the numerical parameters specified in Section III A, we obtain:

$$\theta_0 \approx -1.93592, \quad T \approx 1.97494. \quad (17)$$

The found optimal trajectory is illustrated in Fig. 2 by a white line. The figure also includes trajectories corresponding to small deviations in the initial heading θ_0 and slight perturbations in the initial position \mathbf{r}_A . Overall, these trajectories stay close to the optimal path on the considered time scale and successfully reach a narrow neighborhood of the target point. Based on expressions (15) and (16), it can be concluded that the initial perturbations exhibit linear growth with time rather than exponential growth, indicating only the weak instability of the optimal trajectory.

C. Example 2: Steady sink and time-varying vortex flow

For the background velocity field (3), the Zermelo's equation (14) has a solution $\theta_t = \theta_0 + t/2 - t^2/2$. Then, the equations of motion (1) can be integrated from the starting point $(X_0, Y_0) = (x_A, y_A)$

$$X_t = \frac{e^{-0.3t}}{3} \left[3x_A \cos\left(\frac{t(t-1)}{2}\right) + 3y_A \sin\left(\frac{t(t-1)}{2}\right) + 10V_0(e^{0.3t} - 1) \cos\left(\frac{t(t-1)}{2} - \theta_0\right) \right], \quad (18)$$

$$Y_t = \frac{e^{-0.3t}}{3} \left[3y_A \cos\left(\frac{t(t-1)}{2}\right) - 3x_A \sin\left(\frac{t(t-1)}{2}\right) - 10V_0(e^{0.3t} - 1) \sin\left(\frac{t(t-1)}{2} - \theta_0\right) \right]. \quad (19)$$

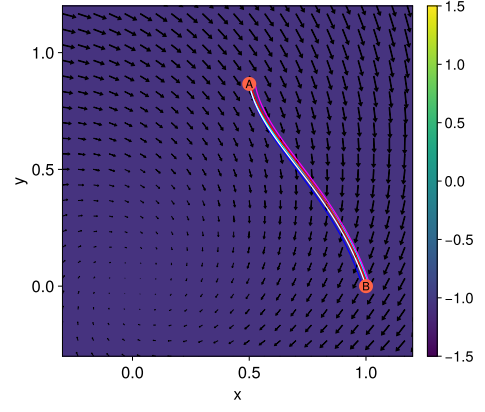


FIG. 3. Optimal control solution (white line) for the steady sink and time-varying vortex flow, see Sections III B. Near-optimal trajectories are shown in cyan and blue for the initial control angle $\theta_0 \pm \pi/360$, and in magenta and red for the initial position error $\Delta = 0.025$ in x_A and y_A .

The found trajectory should also pass through the terminal point $(X_T, Y_T) = (x_B, y_B)$, which allows us to obtain the initial heading θ_0 and travel time T . For the numerical parameters specified in Section III B, we obtain:

$$\theta_0 \approx -0.77543, \quad T \approx 1.03008. \quad (20)$$

Figure 3 presents the optimal trajectory (white line) superimposed on the velocity field at the final time T . The figure also illustrates the system's sensitivity by displaying trajectories with small errors in the initial heading θ_0 and initial position \mathbf{r}_A . All trajectories remain near the optimal path and successfully approach the destination point. The complete time-dependent evolution is provided in the video, see Ref. [28]. Based on expressions (18) and (19), it can be concluded that the initial small perturbations $\delta X_0, \delta Y_0, \delta \theta_0$ do not exhibit growth with time, indicating the neutral stability of the optimal trajectory.

D. Example 3: Taylor-Green vortices

Next, we consider the Taylor-Green flow, see Section III C. Now, the optimal control equations must be solved numerically. To define the problem over a fixed integration interval, it is convenient to introduce a rescaled time variable $\tau = t/T$, such that $\tau \in [0, 1]$. Using this transformation, the governing equations take the form

$$d\hat{X}_\tau/d\tau = u_0T \sin(k\hat{X}_\tau) \cos(k\hat{Y}_\tau) + V_0T \cos(\hat{\theta}_\tau), \quad (21)$$

$$d\hat{Y}_\tau/d\tau = -u_0T \cos(k\hat{X}_\tau) \sin(k\hat{Y}_\tau) + V_0T \sin(\hat{\theta}_\tau), \quad (22)$$

$$d\hat{\theta}_\tau/d\tau = u_0kT [\cos(k\hat{X}_\tau) \cos(k\hat{Y}_\tau) \sin(2\hat{\theta}_\tau) + \sin(k\hat{X}_\tau) \sin(k\hat{Y}_\tau)], \quad (23)$$

where $\hat{\mathbf{R}}_\tau \equiv \mathbf{R}_t$, $\hat{\theta}_\tau \equiv \theta_t$ and the boundary conditions are $(\hat{X}_0, \hat{Y}_0) = (x_A, y_A)$ and $(\hat{X}_1, \hat{Y}_1) = (x_B, y_B)$.

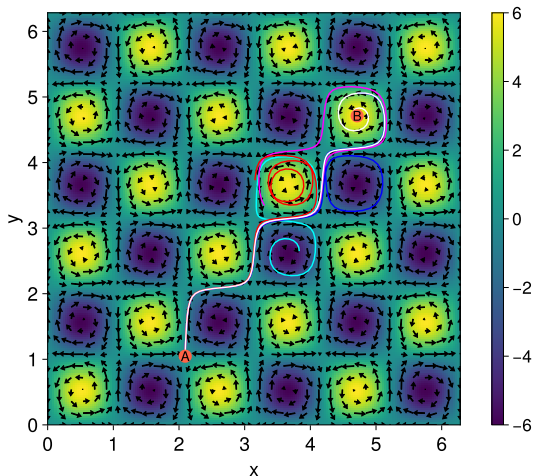


FIG. 4. Optimal control solution (white line) for the Taylor-Green flow, see Sections III C. Perturbed trajectories are shown in cyan and blue for the initial control angle $\theta_0 \pm \pi/9000$, and in magenta and red for the initial position error $\Delta = 10^{-3}$ in x_A and y_A .

The system of equations can be numerically integrated starting from the initial position \mathbf{r}_A for a prescribed initial steering angle θ_0 and total travel time T . However, these two parameters are unknown and must be adjusted so that the final position (\hat{X}_1, \hat{Y}_1) matches the desired target point \mathbf{r}_B . To achieve this, we employ a shooting method followed by fine-tuning optimization. Initially, approximate values of θ_0 and T are chosen to bring the trajectory close to the target. These parameters are then refined to minimize the discrepancy

$$\mathcal{L}(\theta_0, T) = (\hat{X}_1 - x_B)^2 + (\hat{Y}_1 - y_B)^2 \quad (24)$$

between the simulated and desired endpoints. For optimization, we use gradient- and Hessian-based methods. In particular, our implementation first applies the Adam optimizer [49], followed by the BFGS algorithm [50]. Efficient computation of the loss gradients requires the forward integration scheme to support automatic differentiation [51]. Moreover, the integration must be performed with high numerical accuracy. Convergence tests with progressively reduced tolerances are essential to ensure that the solution is independent of the integration precision.

For the numerical parameters specified in Section III C, we obtain:

$$\theta_0 \approx 1.56079, \quad T \approx 12.2038. \quad (25)$$

The corresponding optimal trajectory is shown in Fig. 4 by a white line. The figure also illustrates the system's sensitivity by depicting trajectories perturbed by small deviations in the initial heading $\theta_0 \pm \pi/9000$ and by displacements $\Delta = 10^{-3}$ in the initial x_A and y_A positions. Although these perturbations are considerably smaller than those examined in previous examples, the resulting trajectories fail to reach the target \mathbf{r}_B .

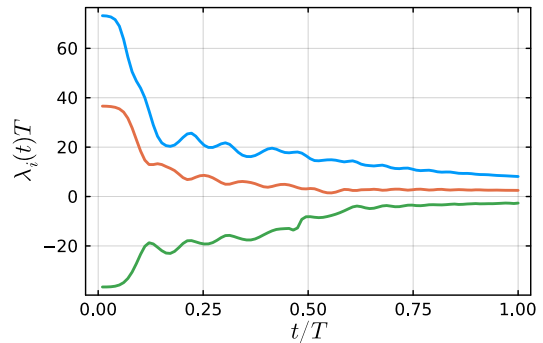


FIG. 5. Normalized FTLEs $\lambda_i T$ for the optimal trajectory found in the Taylor-Green flow.

To make a more quantitative stability analysis of the optimal trajectory, we come back to the original time variable t and consider the evolution of infinitesimal perturbations,

$$(\delta X_t, \delta Y_t, \delta \theta_t)^T = \mathbb{W}(t)(\delta X_0, \delta Y_0, \delta \theta_0)^T, \quad (26)$$

where $\mathbb{W}(t)$ is the linearized evolution matrix that can be obtained numerically. A polar decomposition $\mathbb{W}(t) = \mathbb{V}(t)\mathbb{R}(t)$ allows us to separate the effects of rotation, represented by the orthogonal matrix $\mathbb{R}(t)$, from those of stretching, characterized by the positive-definite matrix $\mathbb{V}(t)$. The eigenvalues $h_i(t)$ of $\mathbb{V}(t)$ (equal to singular values of $\mathbb{W}(t)$) quantify the magnitude of stretching along different directions in phase space and are used to compute the finite-time Lyapunov exponents (FTLEs), defined as

$$\lambda_i(t) = \frac{1}{t} \ln h_i(t), \quad i = 1, 2, 3. \quad (27)$$

The corresponding results are presented in Fig. 5. The presence of a positive maximal FTLE indicates that the optimal trajectory is unstable with respect to small perturbations on the time scales needed to reach the target. This instability limits the practical applicability of the pre-computed optimal control strategy, as minor deviations in initial conditions lead to significant trajectory divergence. Moreover, the resulting sensitivity makes it difficult to find suitable initial guess for parameters θ_0 and T , that lead to a successful solution of the optimization problem and finding optimal trajectories that reach the target. Despite these challenges, computing optimal trajectories can still be practically valuable if the agent additionally employs heuristic strategies to remain near the optimal path [16]. A detailed discussion of such strategies lies beyond the scope of this work.

E. Example 4: Snapshot of 2D Turbulence

Next, we apply the numerical scheme described above to solve the optimal control equations for the steady

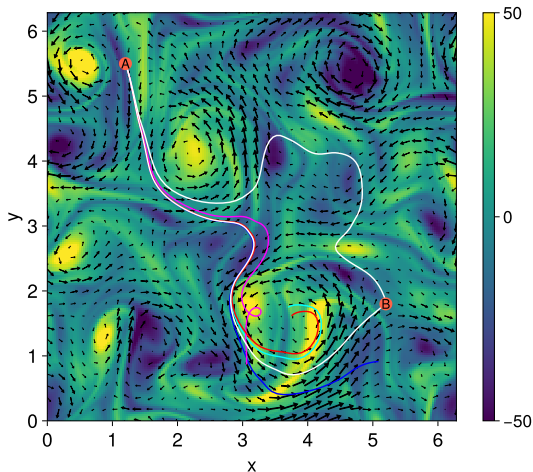


FIG. 6. Two optimal control solutions (white lines) for the snapshot of 2d turbulence, see Sections III D. Perturbed trajectories for the lower path are shown in cyan and blue for the initial control angle $\theta_0 \pm \pi/9000$, and in magenta and red for the initial position error $\Delta = 10^{-3}$ in x_A and y_A .

background flow corresponding to a snapshot of two-dimensional turbulence, see Section III D. The start and end points are chosen as $\mathbf{r}_A = (1.2, 5.5)$ and $\mathbf{r}_B = (5.2, 1.8)$, respectively. Since the optimal trajectory only satisfies the local extremum condition, the resulting equations may, in general, admit multiple solutions. To illustrate this, Fig. 6 presents two distinct optimal trajectories (shown as white lines) corresponding to different initial heading angles θ_0 and total travel times T :

$$\theta_0 \approx -0.883601, \quad T \approx 0.819998, \quad (28)$$

$$\theta_0 \approx -0.863081, \quad T \approx 1.250000. \quad (29)$$

Along the first (lower) trajectory, the agent exploits two vortices encountered on its path to increase speed and reach the target more quickly. In contrast, along the second (upper) trajectory, the agent first uses a nearby vortex to enter a region of weak external flow, where it can maneuver efficiently even with a modest self-propulsion speed V_0 , and then leverages a subsequent current to approach the target. Both trajectories demonstrate effective use of the surrounding flow field, though the first achieves a faster overall transit.

Figure 6 also illustrates the sensitivity of the faster trajectory to small perturbations in the initial control parameter θ_0 and the starting position \mathbf{r}_A . Even minute variations in either of these quantities lead to trajectories that deviate significantly from the optimal path and ultimately fail to reach the target. This observation is further supported by the analysis of FTLEs presented in Fig. 7, where the maximal FTLE attains positive values, confirming that the corresponding trajectory is unstable on the considered time scales. The observed sensitivity to small perturbations reflects an instability in the optimal control dynamics, associated with the agent’s self-propulsion activity [13].

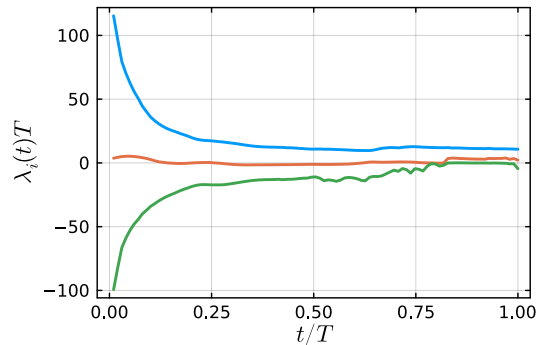


FIG. 7. Normalized FTLEs $\lambda_i T$ for the optimal trajectory found for the snapshot of 2d turbulence.

To better understand this phenomenon, it is instructive to contrast it with the behavior of passive tracers in a steady two-dimensional incompressible flow. For such passive particles, motion occurs strictly along the streamlines, which constrains their trajectories to be regular and precludes the onset of chaotic dynamics. In the present case, however, the agent possesses self-propulsion and an additional degree of freedom associated with the steering direction θ_t , which breaks the integrability of the purely passive system. As a result, the considered active system becomes far more susceptible to chaotic behavior, with small perturbations in initial conditions potentially leading to large deviations in the resulting trajectories.

F. Example 5: 2D Turbulence

In our final example, we consider a background velocity field corresponding to a fully time-dependent two-dimensional turbulent flow, see Section III D. The starting and ending points are set to $\mathbf{r}_A = (1.4, 3.0)$ and $\mathbf{r}_B = (5.2, 1.8)$, respectively. Figure 8 presents the optimal trajectory (depicted as a white line), which corresponds to the initial heading angle θ_0 and total travel time T given by

$$\theta_0 \approx -0.064968, \quad T \approx 0.700001, \quad (30)$$

superimposed on the velocity field at the final time T (a video demonstration is available in Ref. [28]).

This trajectory represents one of potentially many solutions to the optimal control equations, reflecting the existence of multiple local extrema in the optimization landscape. While we cannot prove that the presented solution represents the absolute minimum travel time (i.e., the global optimum), it has been selected for illustration since it yields the shortest travel time among all optimal trajectories identified in our study. As in the previous example, Fig. 8 highlights the sensitivity of the optimal trajectory to small perturbations in the initial conditions – both in the control parameter θ_0 and the starting position \mathbf{r}_A . Even minor deviations in these parameters lead to trajectories that fail to reach the target, emphasizing

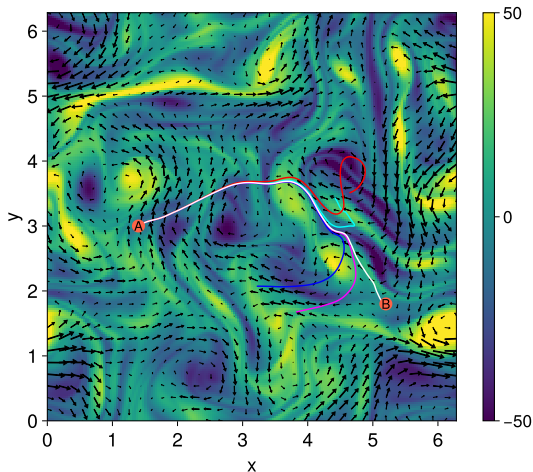


FIG. 8. Optimal control solution (white line) for the full time-dependent 2d turbulent flow, see Sections III D. Perturbed trajectories are shown in cyan and blue for the initial control angle $\theta_0 \pm \pi/9000$, and in magenta and red for the initial position error $\Delta = 10^{-3}$ in x_A and y_A .

the instability and complex structure of the underlying dynamical system. The positive value of the maximal FTLE, shown in Fig. 9, further confirms the trajectory’s instability over the characteristic travel-time scale.

G. Summary

The optimal control framework provides a systematic method for determining time-minimizing trajectories between two points in a fluid flow for an active agent. In simple background flows, these trajectories are robust to small perturbations in initial position and steering direction, making them suitable for practical navigation. Once the initial steering angle θ_0 is set, the agent can autonomously adjust its heading according to Eq. (14), provided it can measure the local velocity field gradients. In more complex flows, finding optimal trajectories becomes considerably more difficult. The resulting paths often exhibit sensitivity to initial conditions and become unstable, limiting the direct application of a naive optimal control strategy in realistic environments. Nevertheless, such trajectories remain valuable. First, the optimal paths reveal how an agent can exploit the structure of the ambient flow to minimize travel time, thereby providing fundamental insight into efficient locomotion strategies. When supplemented with heuristic mechanisms designed to mitigate the influence of environmental noise and modeling uncertainties, these theoretically optimal solutions can still guide the construction of robust navigation algorithms [16]. Second, the optimal trajectories serve as valuable benchmarks: they establish theoretical lower bounds on travel time and offer reference solutions for evaluating the performance of alternative, stability-oriented navigation methods.

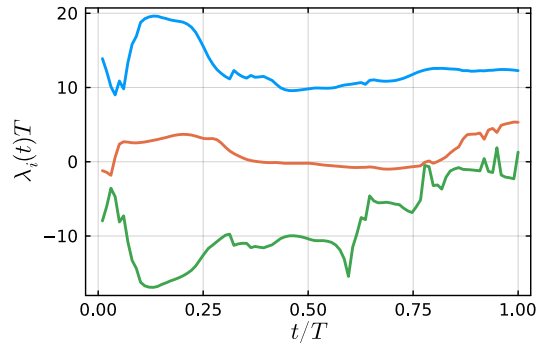


FIG. 9. Normalized FTLEs $\lambda_i T$ for the optimal trajectory found for the full time-dependent 2d turbulent flow.

V. REINFORCEMENT LEARNING

As discussed above, the optimal control approach can be highly sensitive to small perturbations, which limits its robustness in complex flow environments. To overcome this limitation, in this section we employ reinforcement learning (RL) to develop stable navigation strategies. Specifically, we consider two classes of RL algorithms: an action-value method based on Q-learning and a policy-gradient method implemented through a one-step actor-critic framework. We briefly outline the principles of these methods and then apply them to various background flow scenarios, comparing their performance with the optimal control solutions. For a comprehensive introduction to the RL methods employed here, we refer the reader to the classic textbook [27].

A. Action-Value methods: Q-learning

To explain how RL works, we need to introduce the general framework. The agent can move between different states s by performing actions a . It chooses actions a randomly with a probability given by a policy function $\pi(a|s)$, which depends on the current state s . After each action the agent obtains some reward r , so the typical trajectory can be described by the sequence $s_0, a_0, r_1, s_1, a_1, r_2, \dots, s_{T-1}, a_{T-1}, r_T, s_T$, where T denotes the final time step (end of an episode) and s_T is the terminal state. The sum of future rewards is called return $g_t = r_{t+1} + r_{t+2} + \dots + r_T$. The expected return, when starting in s and following π thereafter, is called the value function of state s

$$v_\pi(s) = \mathbb{E}_\pi [g_t | s_t = s]. \quad (31)$$

The closely related concept, central for our discussion, is the action-value function $q_\pi(s, a)$, which determines the expected return, when the agent is in a state s and chooses an action a

$$q_\pi(s, a) = \mathbb{E}_\pi [g_t | s_t = s, a_t = a]. \quad (32)$$

These two objects are related to each other as $v_\pi(s) = \sum_a q_\pi(s, a)\pi(a|s)$.

The agent collects rewards along its way, and the goal is to find the optimal policy $\pi^*(a|s)$ that maximizes the expected cumulative reward over an episode. Action-value methods focus on learning the corresponding function $q_*(s, a)$, which satisfies the Bellman equation:

$$q_*(s, a) = \mathbb{E} \left[r_{t+1} + \max_{a'} q_*(s_{t+1}, a') \mid s_t = s, a_t = a \right]. \quad (33)$$

In Q-learning, $q_*(s, a)$ is approximated iteratively through interaction with the environment using the update rule:

$$Q(s_t, a_t) \leftarrow Q(s_t, a_t) + \alpha \left[r_{t+1} + \max_{a'} Q(s_{t+1}, a') - Q(s_t, a_t) \right], \quad (34)$$

where $Q(s, a)$ is the current approximation for the optimal action-value function and α is the learning rate. This update adjusts the current estimate toward a new target that combines the immediate reward and the best predicted future return. Over many iterations, provided all state-action pairs are adequately explored, $Q(s, a)$ converges to $q_*(s, a)$. The optimal policy is then obtained by selecting, in each state, the action that maximizes the action-value function:

$$\pi^*(a|s) = \begin{cases} 1, & \text{if } a = \operatorname{argmax}_a q_*(s, a), \\ 0, & \text{otherwise.} \end{cases} \quad (35)$$

If the transition from the equation (33) to the update rule (34) appears unclear, Appendix A provides a helpful explanation of the general idea.

A key strength of Q-learning is its off-policy nature: it can learn the optimal policy even while following a different exploratory strategy. To achieve a balance between exploration and exploitation, we employ an ε -greedy protocol. Under this policy, the agent selects the action with the highest estimated value (the greedy action) with probability $1 - \varepsilon$ and a random action with probability ε . A complete pseudocode for the Q-learning algorithm is presented below:

Algorithm: Q-learning

Initialize: $Q(s, a)$ arbitrarily for all states s and actions a , except that $Q(\text{terminal}, \cdot) = 0$

Loop for each episode:

- Initialize starting state $s \leftarrow s_0$
- **Loop for each step of the episode:**
 1. Choose action a from state s using ε -greedy policy derived from Q
 2. Take action a , observe reward r , next state s'
 3. $Q(s, a) \leftarrow Q(s, a) + \alpha [r + \max_{a'} Q(s', a') - Q(s, a)]$
 4. $s \leftarrow s'$

Until the episode is over

Until all episodes are over

Output: $q_*(s, a) \approx Q(s, a)$

B. Policy-Gradient methods: Actor-Critic

We now turn to policy-gradient methods, a family of RL techniques that rely on directly optimizing a parameterized policy. In this approach, the agent's behavior is described by a probability distribution $\pi(a|s, \mathbf{p})$, where \mathbf{p} represents the vector of policy parameters. By smoothly adjusting the components of \mathbf{p} , the agent's policy can be continuously modified. The central objective of such methods is to find the parameters that maximize the expected cumulative reward. This goal can be formalized as maximizing the performance function $J(\mathbf{p}) = v_\pi(s_0)$, where s_0 is the initial state. To achieve this, the parameters are updated using a gradient ascent scheme

$$\mathbf{p}_{t+1} = \mathbf{p}_t + \alpha_p \nabla_{\mathbf{p}} J(\mathbf{p}_t), \quad (36)$$

where α_p denotes the learning rate. The core difficulty lies in computing the gradient $\nabla_{\mathbf{p}} J(\mathbf{p})$.

Fortunately, this gradient can be expressed analytically thanks to the policy gradient theorem, which provides a tractable form for optimization, see Appendix B. According to the theorem,

$$\nabla_{\mathbf{p}} J(\mathbf{p}) \propto \sum_s \mu(s) \sum_a q_\pi(s, a) \nabla_{\mathbf{p}} \pi(a|s, \mathbf{p}), \quad (37)$$

where $\mu(s)$ represents the stationary distribution of states under the policy π . Instead of explicitly averaging over all possible states, the same expression can be interpreted as an expectation over trajectories generated by the policy. Consequently, the gradient can be written as

$$\begin{aligned} \nabla_{\mathbf{p}} J(\mathbf{p}) &\propto \mathbb{E}_\pi \left[\sum_a q_\pi(s_t, a) \nabla_{\mathbf{p}} \pi(a|s_t, \mathbf{p}) \right] \\ &= \mathbb{E}_\pi \left[\sum_a \pi(a|s_t, \mathbf{p}) q_\pi(s_t, a) \frac{\nabla_{\mathbf{p}} \pi(a|s_t, \mathbf{p})}{\pi(a|s_t, \mathbf{p})} \right]. \end{aligned} \quad (38)$$

Next, we can replace the averaging over a with the weight $\pi(a|s_t, \mathbf{p})$ by sampling over a_t generated according to the policy π , and then we can also use the identity $q_\pi(s_t, a_t) = \mathbb{E}_\pi [g_t | s_t, a_t]$ to obtain

$$\nabla_{\mathbf{p}} J(\mathbf{p}) \propto \mathbb{E}_\pi \left[g_t \frac{\nabla_{\mathbf{p}} \pi(a_t | s_t, \mathbf{p})}{\pi(a_t | s_t, \mathbf{p})} \right]. \quad (39)$$

This leads to a practical stochastic gradient ascent rule of the form

$$\mathbf{p}_{t+1} = \mathbf{p}_t + \alpha_p g_t \nabla_{\mathbf{p}} \ln \pi(a_t | s_t, \mathbf{p}_t), \quad (40)$$

where the proportionality constant has been absorbed into the learning rate α_p . The variable g_t represents the total return accumulated from time t onward, implying that parameter updates can only be performed after completing an entire episode. This approach is known as the reinforce algorithm [52].

A notable improvement to the reinforce algorithm involves introducing a baseline term $b(s)$, which helps reduce the variance of the gradient estimate without introducing bias. This modification is justified by the observation that

$$\sum_a b(s) \nabla_{\mathbf{p}} \pi(a|s, \mathbf{p}) = b(s) \nabla_{\mathbf{p}} \sum_a \pi(a|s, \mathbf{p}) = 0, \quad (41)$$

since $\sum_a \pi(a|s, \mathbf{p}) = 1$. Hence, one can replace $q_{\pi}(s, a)$ with $q_{\pi}(s, a) - b(s)$ in the policy gradient theorem (37), leading to the modified update rule

$$\mathbf{p}_{t+1} = \mathbf{p}_t + \alpha_p (g_t - b(s_t)) \nabla_{\mathbf{p}} \ln \pi(a_t|s_t, \mathbf{p}_t). \quad (42)$$

This modification leaves the expected value of the gradient unchanged but may drastically reduce its variance. In practice, an effective choice for the baseline is the state value function itself, $b(s_t) \approx v_{\pi}(s_t)$.

Building upon this idea, the one-step actor-critic algorithm introduces an even more efficient mechanism by replacing g_t with a one-step return. Instead of waiting for the end of an episode, the algorithm uses the estimate $g_t \approx r_{t+1} + v_{\pi}(s_{t+1})$ to compute an immediate update. To make this feasible, the value function is approximated by a differentiable function $V(s, \mathbf{w})$ parameterized by a weight vector \mathbf{w} . The parameters \mathbf{w} are trained to minimize the mean-squared error between the true value function and its approximation $[v_{\pi}(s_t) - V(s_t, \mathbf{w})]^2$ using a stochastic semi-gradient method. The corresponding update rule is

$$\begin{aligned} \mathbf{w}_{t+1} &= \mathbf{w}_t - \frac{\alpha_w}{2} \nabla_{\mathbf{w}} [v_{\pi}(s_t) - V(s_t, \mathbf{w}_t)]^2 \\ &= \mathbf{w}_t + \alpha_w [v_{\pi}(s_t) - V(s_t, \mathbf{w}_t)] \nabla_{\mathbf{w}} V(s_t, \mathbf{w}_t). \end{aligned} \quad (43)$$

Since the true value $v_{\pi}(s_t)$ is unknown, it is replaced with an unbiased estimate based on the observed reward and the value of the next state, $v_{\pi}(s_t) \approx r_{t+1} + V(s_{t+1}, \mathbf{w}_t)$. Strictly speaking, this estimate depends on \mathbf{w}_t , but we ignore this when computing the gradient in the update rule, and for this reason the method is called semi-gradient.

With these definitions, both the policy and the value function parameters can be updated after each interaction step. The resulting learning rules are

$$\begin{aligned} \mathbf{p}_{t+1} &= \mathbf{p}_t + \alpha_p \left[r_{t+1} + V(s_{t+1}, \mathbf{w}_t) \right. \\ &\quad \left. - V(s_t, \mathbf{w}_t) \right] \nabla_{\mathbf{p}} \ln \pi(a_t|s_t, \mathbf{p}_t), \end{aligned} \quad (44)$$

$$\begin{aligned} \mathbf{w}_{t+1} &= \mathbf{w}_t + \alpha_w \left[r_{t+1} + V(s_{t+1}, \mathbf{w}_t) \right. \\ &\quad \left. - V(s_t, \mathbf{w}_t) \right] \nabla_{\mathbf{w}} V(s_t, \mathbf{w}_t). \end{aligned} \quad (45)$$

In this formulation, the first equation adjusts the actor, i.e., the policy $\pi(a|s, \mathbf{p})$ responsible for choosing actions, while the second equation updates the critic, i.e., the value function $V(s, \mathbf{w})$ that evaluates them. The actor learns to favor actions that produce higher-than-expected rewards, guided by the error

$r_{t+1} + V(s_{t+1}, \mathbf{w}_t) - V(s_t, \mathbf{w}_t)$, while the critic improves its estimate of expected returns using the same signal. The critic ‘‘evaluates’’ the actor’s choices, and the actor uses this feedback to refine its policy, reinforcing beneficial actions and discouraging poor ones. A complete pseudocode for the one-step actor-critic algorithm is presented below:

Algorithm: One-Step Actor-Critic

Initialize: Differentiable $\pi(a|s, \mathbf{p})$ and $V(s, \mathbf{w})$ with some initial parameters \mathbf{p} and \mathbf{w} , $V(\text{terminal}, \cdot) = 0$

Loop for each episode:

- Initialize starting state $s \leftarrow s_0$
- **Loop for each step of the episode:**
 1. Choose action a from state s using $\pi(\cdot|s, \mathbf{p})$
 2. Take action a , observe reward r , next state s'
 3. $\mathcal{z} \leftarrow r + V(s', \mathbf{w}) - V(s, \mathbf{w})$
 4. $\mathbf{w} \leftarrow \mathbf{w} + \alpha_w \mathcal{z} \nabla_{\mathbf{w}} V(s, \mathbf{w})$
 $\mathbf{p} \leftarrow \mathbf{p} + \alpha_p \mathcal{z} \nabla_{\mathbf{p}} \ln \pi(a|s, \mathbf{p})$
 5. $s \leftarrow s'$

Until the episode is over

Until all episodes are over

Output: $\pi^*(a|s) \approx \pi(a|s, \mathbf{p})$

Note that once training is complete, we evaluate the learned control in a testing phase by selecting, at each state s_t , the greedy action a_t with the highest probability under the learned policy, i.e. $a_t = \operatorname{argmax}_a \pi(a|s_t, \mathbf{p})$. This deterministic choice allows us to highlight the most likely trajectories implied by the policy, making it easier to visualize and interpret the agent’s characteristic behavior.

C. States, Actions, Rewards

Next, we outline how the general RL framework introduced above can be applied to Zermelo’s navigation problem. The definitions of states, actions and rewards follow Ref. [13], with only minor modifications in our implementation.

The state space is constructed by discretizing the spatial domain $L \times L$ into square tiles or cells s_i , with $i = 1, 2, \dots, N_s$, each of size $\delta \times \delta$. We set $\delta = L/N_{\text{tile}}$, so that in total we have $N_s = N_{\text{tile}}^2$ states. Roughly saying, this coarse graining implies that the agent resolves its position only up to the cell size δ . The agent is allowed to change its steering direction only at discrete time intervals. The duration between them is $\Delta t = \delta/(2u_0)$, where u_0 is taken to be of the order of the maximum flow velocity. The action space is also discretized: the control variable θ_t can take one of $N_a = 8$ equally spaced angles $\theta_j = -\pi + 2\pi j/N_a$ with $j = 1, 2, \dots, N_a$. During each time step of duration Δt , the agent’s trajectory is advanced via numerical integration of the governing equation of motion (1) with the chosen steering angle held fixed.

We define one episode as a single attempt to reach

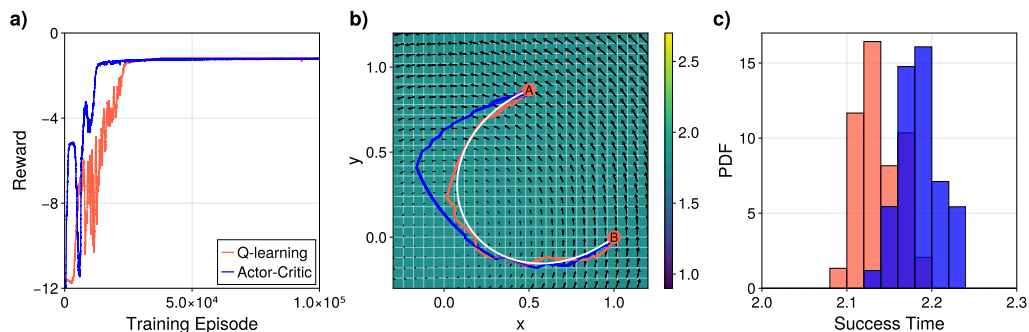


FIG. 10. Example of steady vortex flow, see Section III A. (a) Total reward, averaged over a sliding window of 250 episodes, plotted against the number of training episodes. (b) Trajectories generated by the Q-learning (red) and one-step actor-critic (blue) agents, shown alongside the optimal control trajectory (white). (c) Arrival-time histograms for the trained agents.

the target region. An episode terminates either when the agent enters a circle of radius d_B centered at the target position \mathbf{r}_B , or when a maximum allowed time T_{max} has elapsed. Episodes also terminate prematurely if the agent collides with the domain boundary. Boundary collisions incur an additional negative reward of magnitude $-2T_{max}$, providing a strong penalty that discourages such events. The reward structure is designed to favor short travel times. At each action step, the immediate reward is

$$r_t = -\Delta t + \frac{|\mathbf{r}_B - \mathbf{R}_{t-\Delta t}|}{V_0} - \frac{|\mathbf{r}_B - \mathbf{R}_t|}{V_0}, \quad (46)$$

where V_0 is the slip velocity of the agent and \mathbf{R}_t denotes its position at time t . The first term imposes a constant running cost proportional to time spent, ensuring that long trajectories accumulate a large negative reward. The second and third terms measure the improvement in a distance-based potential and is known to preserve optimality while significantly accelerating convergence during training [13, 25]. When summed over a successfully completed episode (the agent has reached the target), these terms result in a nearly constant addition $\approx |\mathbf{r}_B - \mathbf{r}_A|/V_0$. To enhance robustness with respect to small perturbations of the initial condition, each episode is initialized by sampling the agent's starting point \mathbf{R}_0 uniformly within a circle of radius d_A centered at the nominal initial position \mathbf{r}_A . Throughout this work, we set $d_A = d_B \approx \delta \ll |\mathbf{r}_B - \mathbf{r}_A|$.

In the above formulation, the system state is characterized solely by the agent's spatial position. Although this assumption is appropriate for steady background flows, it may complicate learning or even become restrictive when the flow depends explicitly on time. In such cases, the optimal action at a fixed spatial location can vary as the flow evolves, and a state representation that excludes temporal information may hinder the algorithm's ability to identify optimal trajectories – especially those exhibiting complex features such as self-intersections. Nevertheless, for the time-dependent scenarios examined in this work, we found that RL algorithms employing this reduced state representation can still cope with temporal

variability and successfully learn effective control strategies.

Given the discrete state-action space, with $i = 1, 2, \dots, N_s$ indexing the states and $j = 1, 2, \dots, N_a$ indexing the actions, the action-value function $Q(s, a)$ used in the Q-learning algorithm can be represented explicitly as a matrix Q_{ij} of dimension $N_s \times N_a$. Each entry Q_{ij} corresponds to the estimated value of taking action a_j in state s_i . The policy-gradient methods require specifying a parametric form for the policy $\pi(a|s, \mathbf{p})$, where \mathbf{p} denotes the set of trainable parameters. A convenient and widely used choice is the softmax parameterization:

$$\pi(a_j|s_i, \mathbf{p}) = \frac{\exp(p_{ij})}{\sum_{k=1}^{N_a} \exp(p_{ik})}, \quad (47)$$

where p_{ij} is the (i, j) -th element of an $N_s \times N_a$ parameter matrix. Thus, each state-action pair (s_i, a_j) is associated with a scalar parameter p_{ij} that determines the probability of selecting action a_j when the agent is in state s_i . Finally, for the state-value function we also choose one of the most common parameterizations,

$$V(s_i, \mathbf{w}) = w_i, \quad (48)$$

where w_i is the i -th component of a parameter vector \mathbf{w} of length N_s . This representation assigns one free parameter to each state, keeping the function approximation simple. With these choices, the update rules (44) and (45) for the one-step actor-critic method take the form:

$$\varkappa \leftarrow r + w[s_{t+1}] - w[s_t], \quad (49)$$

$$w[s_t] \leftarrow w[s_t] + \alpha_w \varkappa, \quad (50)$$

$$p[s_t, a_t] \leftarrow p[s_t, a_t] + \alpha_p \varkappa (1 - \pi(a_t|s_t)), \quad (51)$$

$$p[s_t, b \neq a_t] \leftarrow p[s_t, b \neq a_t] - \alpha_p \varkappa \pi(b \neq a_t|s_t). \quad (52)$$

D. Example 1: Steady vortex flow

First, we apply the RL algorithms to the navigation task in the steady vortex flow, see Section III A. The flow domain is restricted to the square $[-0.3, 1.2]^2$, which

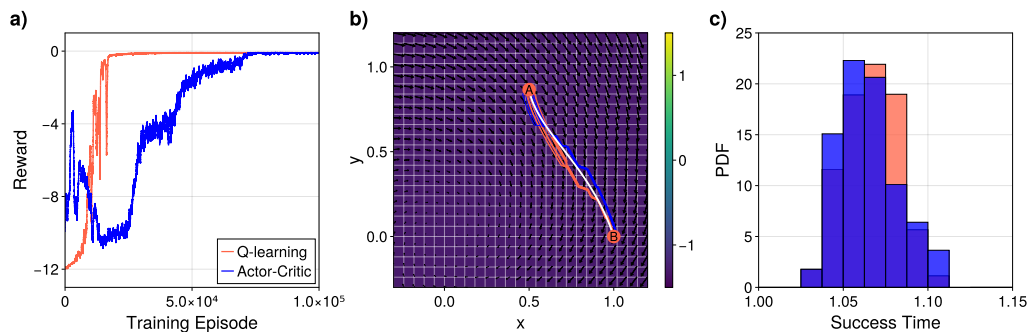


FIG. 11. Example of steady sink and time-varying vortex flow, see Section III B. (a) Total reward, averaged over a sliding window of 250 episodes, plotted against the number of training episodes. (b) Trajectories generated by the Q-learning (red) and one-step actor-critic (blue) agents, shown alongside the optimal control trajectory (white). (c) Arrival-time histograms for the trained agents.

is discretized into $N_s = 25^2$ uniform cells defining the states. The uncertainties in the initial and target points are controlled by $d_A = d_B = 0.04$. Each episode has a maximum duration of $T_{max} = 5$. The agents are trained for $n_{train} = 10^5$ and then evaluated over $n_{eval} = 5 \cdot 10^3$ episodes. In Q-learning, we use a constant learning rate $\alpha = 0.04$ and anneal the policy exploration parameter ε from 1 to 0.01 by multiplying it by 0.9999 after each episode until it reaches the lower bound. In the one-step actor-critic algorithm, the actor and critic learning rates are also constant and set to $\alpha_p = 0.04$ and $\alpha_w = 0.08$, respectively.

The evolution of the total reward $r_{tot} = \sum_t r_t$ during training, averaged over a sliding window of 250 episodes, is shown for both algorithms in Fig. 10a. In each case, the total reward eventually stabilizes, indicating that the learning dynamics have reached a stationary regime and the algorithms have converged. Examples of trajectories obtained from the learned policies are presented in Fig. 10b. For each method, we display ten realizations initialized uniformly at random within a disk of radius d_A centered at \mathbf{r}_A . For reference, the optimal trajectory computed in Section IV B is shown alongside the RL-generated paths. The trajectories produced by Q-learning closely follow the optimal control solution; the small deviations that remain can be attributed primarily to the discretization inherent in our RL formulation. In contrast, the one-step actor-critic method yields trajectories that exhibit systematic deviations from the optimal path. These deviations are robust: they persist across independent training runs and remain even after varying the training hyperparameters. Apparently, this behavior can be related to the on-policy nature of the one-step actor-critic algorithm, which may converge to local minimum of the policy-gradient landscape.

The performance difference between the two methods is illustrated by the arrival-time statistics shown in Fig. 10c. All evaluated trajectories reach the target, implying that both methods achieve a zero failure rate. However, the Q-learning agent achieves a slightly shorter mean travel time, $\langle T \rangle \approx 2.14$, compared with $\langle T \rangle \approx 2.18$

for the one-step actor-critic agent. Therefore, while both RL approaches successfully solve the navigation task, Q-learning provides a closer approximation to the optimal control solution and delivers better performance, but the difference in mean travel time amounts to a few percent.

E. Example 2: Steady sink and time-varying vortex flow

Next, we apply the Q-learning and one-step actor-critic algorithms to the navigation task in the steady sink and time-dependent vortex flow, see Section III B. The training hyperparameters are identical to those used in the previous example, except that for the one-step actor-critic method we slightly increase the learning rates to $\alpha_p = 0.05$ for the actor and $\alpha_w = 0.1$ for the critic. The corresponding results are summarized in Fig. 11.

Both algorithms converge successfully in this time-dependent external flow, as illustrated in Fig. 11a, despite the fact that the state representation relies solely on the agent's position. The trajectories produced by the learned policies are reasonably close to the optimal control solution derived in Section IV C, see Fig. 11b. A visualization of the full time-dependent evolution is available in the videos provided in Ref. [28]. All evaluated trajectories reach the target, demonstrating a zero failure rate for both approaches. The arrival-time statistics in Fig. 11c indicate that the two algorithms perform comparably, with mean travel times of approximately $\langle T \rangle \approx 1.065$.

F. Example 3: Taylor-Green vortices

The next example concerns the Taylor-Green flow described in Section III C. The flow domain $[0, 2\pi]^2$ is discretized into $N_s = 30^2$ uniform square cells that define the state space. The uncertainties in the initial and target positions are set to $d_A = d_B = 0.2$. The maximum episode duration is given by $T_{max} = 2|\mathbf{r}_B - \mathbf{r}_A|/V_0$, where

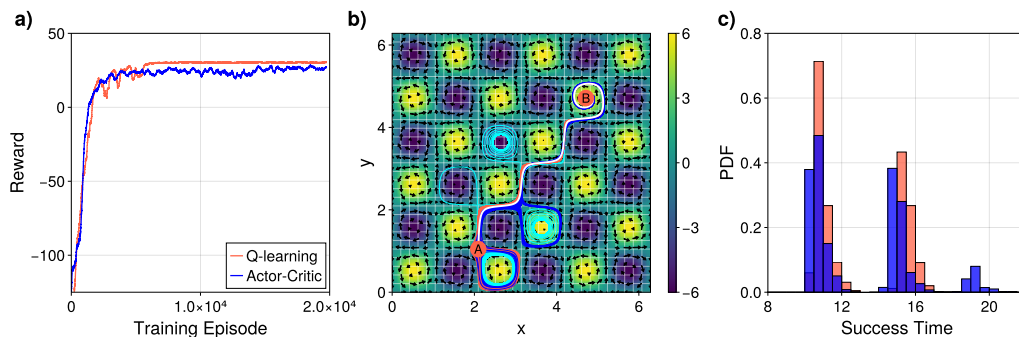


FIG. 12. Example of Taylor-Green flow, see Section III C. (a) Total reward, averaged over a sliding window of 250 episodes, plotted against the number of training episodes. (b) Trajectories generated by the Q-learning (red) and one-step actor-critic (blue) agents, together with those obtained using the trivial policy (cyan) are shown alongside the optimal control trajectory (white). (c) Arrival-time histograms for the trained agents.

$V_0 = 0.1$ denotes the agent’s self-propulsion speed. The agents are trained for $n_{train} = 2 \cdot 10^4$ and then evaluated over $n_{eval} = 5 \cdot 10^3$ episodes. In Q-learning, we employ a constant learning rate of $\alpha = 0.04$ and anneal the policy exploration parameter ε from 1 to 0.01 by multiplying it by 0.9995 after each episode until the lower bound is reached. For the one-step actor-critic method, the actor and critic learning rates are also constant and set to $\alpha_p = 0.005$ and $\alpha_w = 0.01$, respectively.

Figure 12a shows the learning curves obtained for the Q-learning and one-step actor-critic algorithms. In both cases, the curves level off at relatively high total rewards, indicating that each method successfully learns an effective control policy. Representative trajectories generated by the learned policies are displayed in Fig. 12b, alongside the optimal control path computed in Section IV D. As illustrated, the Q-learning agent typically proceeds directly toward the target along a route close to the optimal one, although it may complete a single revolution around a nearby vortex when its initial state makes immediate escape impossible. The actor-critic agent performs less reliably: in addition to this initial revolution, it is sometimes captured by a second vortex, which forces an additional turn.

These observations are further supported by the arrival-time statistics shown in Fig. 12c. The first peak corresponds to near-optimal trajectories; the second arises from trajectories that include one extra loop within a Taylor-Green vortex; and the third reflects trajectories with two such additional rotations. Because of uncertainty in the initial position and the larger size of the target region, some trajectories terminate faster than the optimal-control prediction (25). Note that all tested trajectories for both RL algorithms arrive at the target, yielding a zero failure rate. The appearance of the third peak leads to a slightly longer mean travel time for the actor-critic agent, $\langle T \rangle \approx 13.1$, compared with $\langle T \rangle \approx 12.9$ for the Q-learning agent. However, this difference is only a few percent, and overall both algorithms solve the task successfully.

For comparison, we have also implemented a trivial

policy, where the steering angle selected by the agent at each Δt is given by the action that points most directly toward the target among the $N_a = 8$ different possibilities. In this case, the agent reaches the target with a probability of only ≈ 0.3 , depending on its random starting position. In the remaining trials, the agent becomes trapped in Taylor-Green vortices, from which this naive strategy cannot escape, as illustrated by the cyan trajectories in Fig. 12b.

G. Example 4: Snapshot of 2D Turbulence

Next, we apply the RL algorithms to a navigation task in the steady velocity field obtained from a snapshot of two-dimensional turbulence, see Section III D. The flow domain $[0, 2\pi]^2$ is discretized into $N_s = 30^2$ uniform square cells, which serve as the state space. Uncertainty in both the initial and target positions is characterized by $d_A = d_B = 0.2$. The maximum episode duration is set to $T_{max} = 5|\mathbf{r}_B - \mathbf{r}_A|/V_0$, where V_0 is the agent’s self-propulsion speed. Agents are trained for $n_{train} = 10^5$ episodes and evaluated over an additional $n_{eval} = 5 \cdot 10^3$ episodes. For Q-learning, we use a constant learning rate $\alpha = 0.04$ and gradually reduce the policy exploration parameter ε from 1 to 0.01 by multiplying it by 0.9999 at the end of each episode until the lower bound is reached. For the one-step actor-critic algorithm, the actor and critic learning rates are kept constant at $\alpha_p = 0.005$ and $\alpha_w = 0.01$, respectively.

Figure 13a shows the evolution of the total reward throughout training. For both RL algorithms, the learning curves level off, indicating convergence. Representative trajectories generated by the learned policies are displayed in Fig. 13b, together with the optimal control trajectory from Section IV E. As seen in the figure, the actor-critic agent’s trajectories closely track the optimal control path, whereas the Q-learning trajectories exhibit small deviations in the latter part of the journey. Consistently, the actor-critic agent achieves a shorter average travel time, $\langle T \rangle \approx 0.87$, compared with $\langle T \rangle \approx 0.96$ for

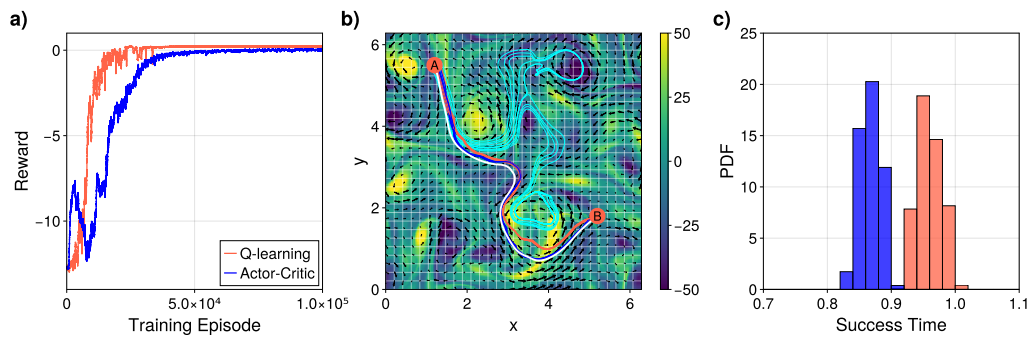


FIG. 13. Example of 2d turbulence snapshot, see Section III D. (a) Total reward, averaged over a sliding window of 250 episodes, plotted against the number of training episodes. (b) Trajectories generated by the Q-learning (red) and one-step actor-critic (blue) agents, together with those obtained using the trivial policy (cyan) are shown alongside the optimal control trajectory (white). (c) Arrival-time histograms for the trained agents.

the Q-learning agent, see Fig. 13c.

This difference does not contradict the observation in Fig. 13a, where the Q-learning agent attains a higher total reward at the end of training. The discrepancy arises because, during evaluation, the actor-critic agent selects the most probable actions from the learned policy, which yield higher rewards and consequently shorter travel times. Overall, all evaluated trajectories successfully reach the target, demonstrating a zero failure rate for both algorithms. Nonetheless, in the considered example the one-step actor-critic method provides a closer approximation to the optimal control solution and delivers better performance. Note also that the trivial policy completely fails to solve the considered navigation task, yielding a failure rate of unity. Under this strategy, the agent eventually enters regions where the external flow cancels its self-propulsion, causing it to stall, see the cyan trajectories in Fig. 13b. As a result, it becomes effectively immobilized and fails to reach the target.

H. Example 5: 2D Turbulence

In our final example, we consider navigation in a time-dependent 2d turbulent flow, see Section III D. The training hyperparameters are identical to those used for the steady 2d turbulence snapshot, except the tuned learning rates. Specifically, now the Q-learning algorithm uses a learning rate of $\alpha = 0.01$, while the one-step actor-critic method employs learning rates of $\alpha_p = 0.04$ for the actor and $\alpha_w = 0.08$ for the critic. The obtained results are summarized in Fig. 14.

Both methods converge, as indicated by the learning curves in Fig. 14a. However, the learned policies differ substantially, which is reflected in the distinct trajectories followed by the trained agents, see Fig. 14b. The Q-learning agent follows a path that is close to the solution obtained within optimal control theory in Section IV F. The latter part of this trajectory passes through a region of weak background flow, which the agent is able to overcome by executing well-coordinated maneuvers. As

can be observed in the demonstration video provided in Ref. [28], the Q-learning agent selects suboptimal motion directions near the very end of the episode, resulting in a noticeable increase in the mean travel time $\langle T \rangle \approx 0.096$ compared to $\langle T \rangle \approx 0.07$ for the optimal control solution, see Eq. (30).

The actor-critic agent, by contrast, follows a different route. It identifies a strong background current directed toward the target and successfully exploits it. This strategy yields a mean travel time of $\langle T \rangle \approx 0.097$, which is comparable to the performance of the Q-learning agent. Both methods exhibit a zero failure rate, and the corresponding arrival-time statistics are presented in Fig. 14c. Qualitatively, the observed behavior of the agents is similar to the navigation task in a steady vortex flow, where different RL methods also discover distinct trajectories with comparable performance, see Section V D. In both examples, the trajectories discovered by the Q-learning agent more closely resemble the theoretic optimal control solution to the navigation problem.

Finally, we examine a trivial policy for the 2d turbulent flow example. This policy fails to reach the target in the majority of runs, with a failure rate of approximately 0.95. Even in the rare cases where it succeeds, the travel time is excessively long and the resulting trajectories are far from optimal. Figure 14b shows representative trajectories for this policy, depicted in cyan. The low self-propulsion speed of the agent prevents it from overcoming the external currents and reaching the target.

VI. INCOMPLETE FLOW INFORMATION

So far, we have seen that RL algorithms successfully solve navigation problems in various background flows with zero failure rate and exhibit strong robustness to perturbations in the agent's initial position. These results suggest that RL methods may also remain stable under small fluctuations in the external velocity field that may arise, among other reasons, from incomplete information about the surrounding flow. This aspect is par-

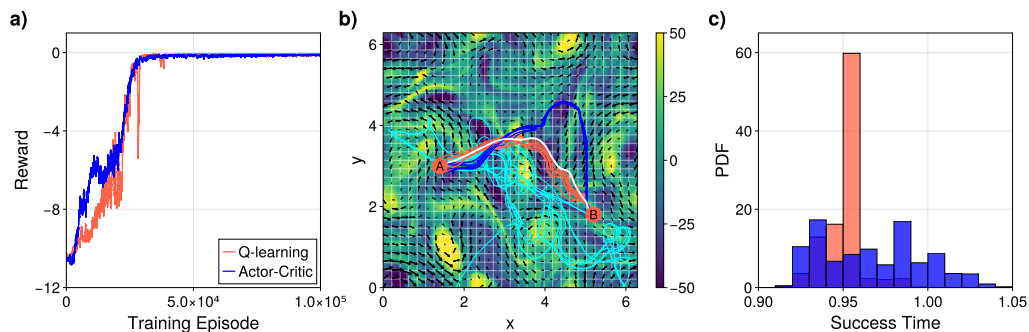


FIG. 14. Example of time-dependent 2d turbulent flow, see Section III D. (a) Total reward, averaged over a sliding window of 250 episodes, plotted against the number of training episodes. (b) Trajectories generated by the Q-learning (red) and one-step actor-critic (blue) agents, together with those obtained using the trivial policy (cyan) are shown alongside the optimal control trajectory (white). (c) Arrival-time histograms for the trained agents.

ticularly crucial for predicting movement in real atmospheric or oceanic environments, where small-scale turbulent fluctuations are difficult to forecast. In this section, we examine this issue in detail.

A. Methodology

In two-dimensional turbulent flows, most of the kinetic energy is concentrated at large spatial scales, see Fig. 1. In the inverse energy cascade range, $k < k_f$, where k_f denotes the forcing wavenumber, the energy spectrum follows the scaling $E(k) \propto k^{-5/3}$. Consequently, the characteristic velocity associated with motions of size r can be estimated as $v_r \sim (\epsilon r)^{1/3}$, where ϵ is the energy flux in the inverse cascade or, equivalently, the power injected into the system [15]. The characteristic timescale for velocity variations at scale r then becomes $t_r \sim r/v_r \sim \epsilon^{-1/3} r^{2/3}$. Thus, the energetically dominant large scales evolve slowly and are relatively easy to predict, whereas small-scale fluctuations change rapidly and are inherently difficult to forecast with precision.

In what follows, we assume that the agent has access to an accurate prediction of all flow modes with wavenumbers $k \leq k_{max}$, while possessing no information about the smaller-scale fluctuations. Practically, this means that we take the velocity field produced by the DNS and remove all Fourier modes with $k > k_{max}$. By varying the filtering threshold k_{max} , we can directly control the amount of flow information available to the agent.

We then train the agent using RL algorithms on this coarse-grained flow field and determine the resulting navigation strategies. Finally, we evaluate these strategies in the full velocity field to assess whether the agent can still successfully reach its target when exposed to the previously unseen small-scale fluctuations. Below, we examine two representative navigation scenarios: one in a steady snapshot of the 2d turbulent flow, and another in the fully time-dependent 2d turbulent field. In our examples, the forcing scale is fixed at $k_f = 5.5$, and we progressively reduce the filtering scale, considering

$k_{max} = \{256, 10, 5, 3, 2\}$. Note that $k_{max} = 256$ corresponds to the fully resolved DNS velocity field.

The performance of the agents is quantified using two primary metrics: the fraction of attempts that successfully reach the target and the mean travel time of those successful attempts. Both quantities are analyzed as functions of the normalized filtering scale k_{max}/k_f . For each value of k_{max} and for each RL algorithm, we perform $n = 10$ independent training runs and report averages over these runs to reduce variability due to stochastic training effects. The mean success probability is defined as

$$\langle p \rangle = \frac{1}{n} \sum_{i=1}^n p_i, \quad (53)$$

where p_i denotes the success probability obtained in the i -th training run. The mean travel time, computed over successful trajectories only, is given by

$$\langle T \rangle = \sum_{i=1}^n g_i \langle T \rangle_i, \quad g_i = \frac{p_i}{\sum_{k=1}^n p_k}, \quad (54)$$

where $\langle T \rangle_i$ is the mean travel time of successful episodes in run i , and the weights g_i ensure that runs with higher success rates contribute proportionally more to the overall average. In addition to the mean values, we report the estimated standard deviations of both metrics across independent training runs. These fluctuations provide a quantitative measure of the robustness and reproducibility of agent performance with respect to stochasticity in the training procedure.

B. Example 1: Snapshot of 2D Turbulence

We first study the navigation problem in a single snapshot of the 2d turbulent flow. For all filtering scales k_{max} , the training hyperparameters for both the Q-learning and one-step actor-critic algorithms are identical to those employed in Section V G. Representative trajectories of

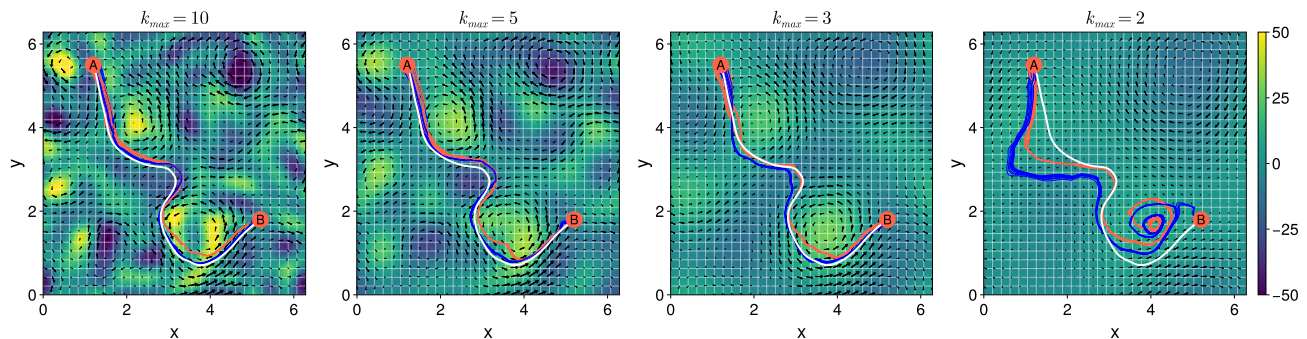


FIG. 15. Trajectories produced by the Q-learning (red) and one-step actor-critic (blue) agents are shown together with the optimal control trajectory (white) for the 2d turbulence snapshot. The background depicts the coarse-grained velocity field, retaining only modes with wavenumbers $k \leq k_{max}$, which was used during training. All trajectories, however, were evaluated in the full (unfiltered) velocity field.

agents trained in coarse-grained flows are illustrated in Fig. 15. The analysis of the success probability $\langle p \rangle$ and the mean travel time $\langle T \rangle$ is provided in Fig. 16.

The learned policies remain reliable when the filtering scale satisfies $k_{max} \geq 3$. In this regime, both RL algorithms guide the agent toward the target along trajectories that closely resemble the optimal control solution, see Fig. 15. Consistent with our earlier observations, the one-step actor-critic algorithm outperforms Q-learning for the 2d turbulence snapshot example. It reaches the target with unit success probability, $\langle p \rangle = 1$, across ten independent training runs and yields a smaller mean travel time $\langle T \rangle$, see Fig. 16. By contrast, the Q-learning agent is less robust. For $k_{max} = 5$ and $k_{max} = 3$, training fails in approximately one out of ten independent runs, in which case the agent is unable to find a path to the target. Even in successful runs, the mean travel time is larger than that of the actor-critic agent, and the variability across different trained models is higher. Notably, the stochasticity of the training process increases as k_{max} decreases, reflecting the growing loss of information in the

filtered velocity field.

When the filtering becomes more severe, at $k_{max} = 2$, the behavior changes qualitatively. The Q-learning agent completely fails to reach the target, resulting in a vanishing success probability, $\langle p \rangle = 0$. The actor-critic agent performs better, achieving success in roughly 50% of the trials; however, its mean travel time nearly doubles compared to models trained on velocity fields that retain more spectral content. Consequently, the agent trajectories deviate markedly from the optimal control solution, see the right panel in Fig. 15. Thus, the removal of velocity modes with wavenumbers $k > 2$ leads to a substantial distortion of the flow structure. At this level of coarse graining, the available information becomes insufficient for effective learning, rendering the resulting control policies largely impractical.

C. Example 2: 2D Turbulence

The next example focuses on a navigation problem in time-dependent 2d turbulent flow. For all filtering scales k_{max} , the training hyperparameters for both the Q-learning and one-step actor-critic methods are selected to be identical to those used earlier in Section V H. Representative trajectories of agents trained in coarse-grained flows are shown in Fig. 17. The corresponding statistical analysis of the success probability $\langle p \rangle$ and the mean travel time $\langle T \rangle$ is presented in Fig. 18.

The obtained results indicate that both algorithms are capable of solving the navigation task for a moderate level of coarse-graining $k_{max} \geq 3$. The one-step actor-critic approach exhibits a high success probability $\langle p \rangle \approx 1$. This is because the trajectories discovered by the agent exploit a strong background current directed toward the target, which does not require highly coordinated control actions. In contrast, the Q-learning agent follows trajectories that pass through a region of weak external flow, where successful navigation demands a more coordinated sequence of actions. As a result, the probability of reaching the target is lower, but the success-

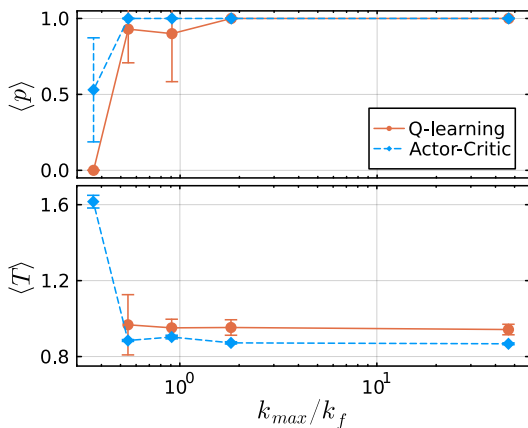


FIG. 16. The success rate (top) and the mean travel time (bottom) vs. normalized filtering scale k_{max}/k_f for the 2d turbulence snapshot example. Error bars indicate the standard deviation.

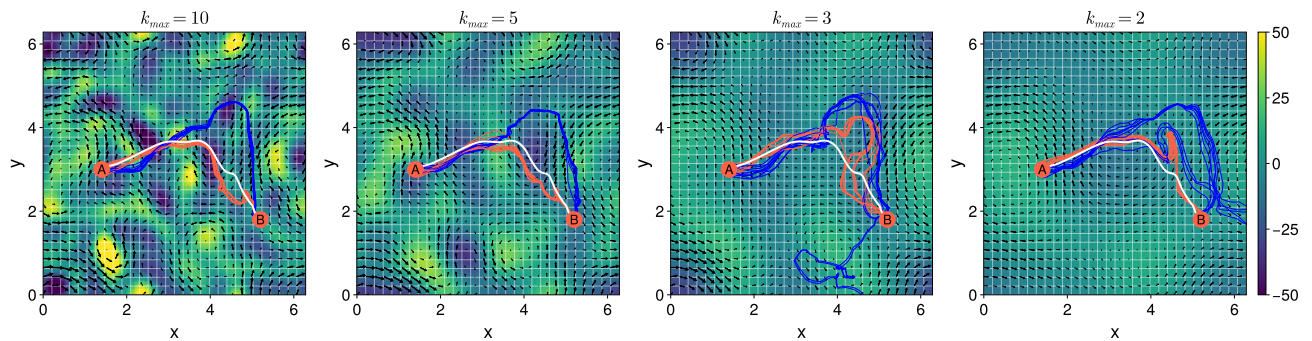


FIG. 17. Trajectories produced by the Q-learning (red) and one-step actor-critic (blue) agents are shown together with the optimal control trajectory (white) for the time-dependent 2d turbulent flow. The background depicts the coarse-grained velocity field, retaining only modes with wavenumbers $k \leq k_{max}$, which was used during training. All trajectories, however, were evaluated in the full (unfiltered) velocity field.

ful trajectories are closer to the theoretical solution predicted by optimal control theory and yield a smaller mean travel time, see Fig. 18.

Upon further increasing the coarse-graining scale to $k_{max} = 2$, the success probability of the actor-critic algorithm drops sharply. This degradation is attributed to the strong fluctuations arising from unresolved velocity-field scales. The Q-learning algorithm, on the other hand, exhibits the opposite behavior: its probability of successfully reaching the target increases and approaches $\langle p \rangle \approx 1$. This behavior appears to result from a fortuitous alignment of circumstances: the policy learned in the coarse-grained flow is more robust to external noise and leads to a shorter mean travel time. We believe that this counterintuitive outcome is specific to the particular example considered here (the choice of initial and target locations). In more general settings, one would expect a reduced success probability and increased travel times, consistent with the trend observed when varying k_{max} from 10 down to 3.

Summarizing the results of this and the preceding

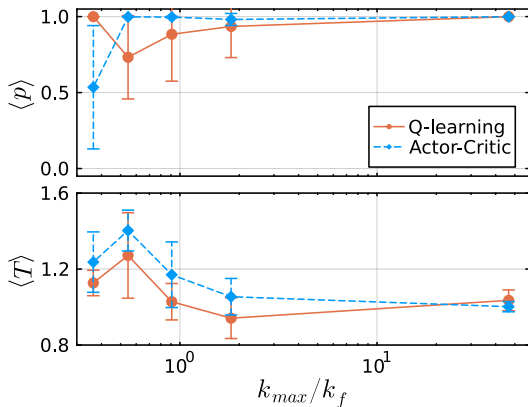


FIG. 18. The success rate (top) and the mean travel time (bottom) vs. normalized filtering scale k_{max}/k_f for the time-dependent 2d turbulent flow. Error bars indicate the standard deviation.

example, we observe that the trajectories produced by the RL algorithms exhibit a degree of robustness to the absence of small-scale velocity-field information. However, once the filtering scale approaches the characteristic size of the flow structures that govern the agent’s route selection, the performance of RL methods deteriorates markedly. Our results suggest that, for two-dimensional turbulence, the critical filtering scale k_{max} is smaller than the characteristic forcing wavenumber k_f and lies within the inverse energy cascade range.

VII. CONCLUSION

In this work, we conducted a systematic investigation of optimal navigation in two-dimensional flows of increasing dynamical complexity, ranging from steady solid-body rotation to fully developed turbulence in the inverse energy cascade regime. Using optimal control theory, we demonstrated that time-minimizing trajectories can be computed accurately even in complex environments; however, their practical applicability becomes limited in complex flows due to strong sensitivity to initial conditions and the instability of the resulting optimal paths. The presence of an additional degree of freedom associated with the steering direction makes the active system more susceptible to chaotic behavior than a passive scalar. In particular, this manifests as an exponential divergence of initially nearby trajectories of an active agent in some two-dimensional incompressible stationary velocity fields.

To overcome the instability of optimal trajectories and identify stable behavioral strategies for agents, we employed RL as an alternative capable of adapting to complex flow structures. By comparing two canonical classes of RL algorithms – action-value (Q-learning) and policy gradient (one-step actor-critic) methods – we showed that both approaches produce robust navigation strategies across all considered flow configurations. The resulting agent trajectories do not always coincide for the two RL algorithms, and our analysis indicates that the Q-

learning typically produces outcomes that more closely resemble the theoretical optimal control solutions.

A key result of our study is the strong generalization capability of RL agents trained on coarse-grained turbulent velocity fields. Agents exposed only to large-scale flow information were nevertheless able to navigate efficiently within the full turbulent environment. This robustness to missing small-scale data is particularly promising for real-world applications, where environmental forecasts are typically low-resolution and subject to uncertainty. Importantly, the success of RL in this setting appears to stem less from algorithmic complexity than from the physical structure of the flow itself.

The framework presented here also offers a flexible platform for future studies. The use of deep RL, where action-value functions and policies are represented by neural networks, would eliminate the need for state-action discretization and enable navigation in more complex settings or higher-dimensional velocity fields. Next, the objective functional itself can be generalized: besides minimizing travel time, one may incorporate additional criteria such as energy expenditure, fuel consumption, or multi-objective trade-offs between efficiency and safety. Another important direction of research can be related to more realistic agent models. Incorporating inertia, turning-rate limitations and stochastic forcing representing environmental noise would further bridge the gap between theory and practical deployment [16, 20, 24].

From a methodological perspective, the coexistence of ground truth optimal-control solutions and RL-based strategies within the same testbed creates a rare opportunity. It allows quantitative comparison between exact minimum-time trajectories and learned policies in data-driven control. Because the navigation problem is physically transparent, the framework is also well suited for use in teaching, providing an accessible setting in which students can explore nonlinear dynamics, turbulent transport, and modern machine-learning techniques within a unified context.

Overall, our findings demonstrate that RL provides a powerful framework for navigation in complex flow environments, complementing classical optimal control theory and overcoming its primary limitations in chaotic regimes. These results open the door to developing practical autonomous navigation strategies for micro-robots, underwater vehicles, and other active agents operating in realistic oceanic and atmospheric flows.

ACKNOWLEDGMENTS

The work was supported by the Ministry of Science and Higher Education of the Russian Federation and by the Basic research program of HSE University. I am also grateful to the Landau Institute for providing computing resources.

Appendix A: Incremental update

Assume for a moment that we are interested in estimating the mean value of a random number generator. At each step, we obtain a single sample, and just before the n -th step, our estimate of the mean is given by

$$Q_n = \frac{r_1 + r_2 + \dots + r_{n-1}}{n-1}. \quad (\text{A1})$$

From this definition, one can derive a recursive update rule that allows computing the next estimate without explicitly storing all past samples:

$$Q_{n+1} = Q_n + \frac{1}{n}(r_n - Q_n), \quad (\text{A2})$$

where $Q_1 = 0$. The main advantage of this incremental form is its computational efficiency: instead of maintaining the entire history of samples, we only need the current estimate Q_n and the most recent observation r_n . Each new sample slightly adjusts the estimate in the direction of the new data point, with the step-size determined by $1/n$.

More generally, this recursive formulation can be expressed in the abstract form

$$\begin{aligned} \text{New Estimate} \leftarrow & \text{Old Estimate} + \\ & \alpha (\text{Target} - \text{Old Estimate}), \end{aligned} \quad (\text{A3})$$

where the target represents a potentially noisy indicator of the true value toward which the estimate should move, and α is the step-size or learning rate that controls how strongly the estimate is updated. In the present case, the target corresponds to the new sample r_n , and the learning rate is $\alpha = 1/n$. Because this learning rate decays over time, each update becomes smaller, which guarantees convergence of Q_n to the true mean as $n \rightarrow \infty$ in accordance with the law of large numbers, see Eq. (A1).

The choice of learning rate schedule determines how the estimate responds to new data. When a decaying learning rate $\alpha = 1/n$ is used, all samples contribute equally to the final estimate. This approach is suitable when the underlying random process is stationary. If, on the other hand, the process is non-stationary and its statistical properties vary with time, assigning equal weight to all past samples may be sub-optimal. In such cases, it is preferable to emphasize more recent observations by using a constant learning rate $\alpha = \text{const}$. With a constant learning rate, the estimate can be written as

$$Q_{n+1} = \sum_{i=1}^n \alpha (1-\alpha)^{n-i} r_i, \quad (\text{A4})$$

which corresponds to an exponentially weighted moving average where more recent samples have greater influence. This formulation enables the estimate to adapt to changing conditions, but it also introduces persistent fluctuations around the true mean due to the most recent

samples. The magnitude of these fluctuations decreases as the learning rate becomes smaller, at the cost of slower adaptation to new information.

In practice, choosing an appropriate learning rate or decay schedule involves balancing adaptability and stability. If the learning rate decays too quickly, the estimate may become insensitive to new data; if it decays too slowly, convergence to the true mean may not occur. Modern machine learning algorithms address this trade-off through adaptive learning rate methods, such as Adam [49], RMSProp [53], or Adagrad [54], which automatically adjust the effective step-size based on the observed variance of updates, see also Ref. [55]. These methods generalize the simple recursive rule presented above and form the foundation of many contemporary optimization techniques.

Appendix B: Policy Gradient Theorem

The proof of the policy gradient theorem presented here follows closely the derivation given in Ref. [27], and is included for completeness. Throughout the derivation, we assume that the policy $\pi(a|s)$ depends on a parameter vector \mathbf{p} , and all gradients are taken with respect to these parameters. For notation compactness, this dependence is left implicit.

For any state s , the state-value function can be expressed in terms of the action-value function as $v_\pi(s) = \sum_a q_\pi(s, a)\pi(a|s)$. Taking the gradient of this expression yields

$$\nabla v_\pi(s) = \sum_a [\nabla\pi(a|s)q_\pi(s, a) + \pi(a|s)\nabla q_\pi(s, a)]. \quad (\text{B1})$$

To evaluate the second term, we represent the action-value function in terms of the environment's transition dynamics. Given the joint probability $p(s', r|s, a)$ of reaching state s' and receiving reward r after taking action a in state s , the function $q_\pi(s, a)$ can be written as

$$q_\pi(s, a) = \sum_{s', r} p(s', r|s, a)(r + v_\pi(s')). \quad (\text{B2})$$

Since the environment's transition model does not depend on the policy parameters, differentiation gives

$$\nabla q_\pi(s, a) = \sum_{s'} p(s'|s, a)\nabla v_\pi(s'), \quad (\text{B3})$$

where $p(s'|s, a) = \sum_r p(s', r|s, a)$ denotes the marginal transition probability. Substituting Eq. (B3) into

Eq. (B1) leads to a recursive form,

$$\nabla v_\pi(s) = \sum_a \left[\nabla\pi(a|s)q_\pi(s, a) + \pi(a|s) \sum_{s'} p(s'|s, a)\nabla v_\pi(s') \right]. \quad (\text{B4})$$

The term involving $\nabla v_\pi(s')$ can itself be expanded using Eq. (B4), and this substitution can be applied recursively to capture contributions from all future states along a trajectory generated by the policy. After the first substitution, we obtain

$$\begin{aligned} \nabla v_\pi(s) = & \sum_a \left[\nabla\pi(a|s)q_\pi(s, a) \right. \\ & + \pi(a|s) \sum_{s'} p(s'|s, a) \sum_{a'} \left[\nabla\pi(a'|s')q_\pi(s', a') \right. \\ & \left. \left. + \pi(a'|s') \sum_{s''} p(s''|s', a')\nabla v_\pi(s'') \right] \right]. \end{aligned} \quad (\text{B5})$$

Carrying out this expansion indefinitely yields an infinite series representing the influence of all possible state transitions:

$$\nabla v_\pi(s) = \sum_x \sum_{k=0}^{\infty} P(s \rightarrow x, k, \pi) \sum_a \nabla\pi(a|x)q_\pi(x, a), \quad (\text{B6})$$

where $P(s \rightarrow x, k, \pi)$ denotes the probability of reaching state x from s in exactly k steps under policy π . For instance, $P(s \rightarrow x, 1, \pi) = \sum_a p(x|s, a)\pi(a|s)$.

The overall performance objective of the policy is defined as $J(\mathbf{p}) = v_\pi(s_0)$, where s_0 is the initial state (or drawn from an initial distribution). Taking the gradient of this quantity and substituting the above expansion, we obtain

$$\nabla J(\mathbf{p}) = \sum_s \left(\sum_{k=0}^{\infty} P(s_0 \rightarrow s, k, \pi) \right) \sum_a \nabla\pi(a|s)q_\pi(s, a). \quad (\text{B7})$$

The inner summation represents the expected visitation frequency of state s , which is proportional to the stationary distribution of states $\mu(s)$ under policy π . Using this notation, the gradient of the performance objective can be written in the form

$$\nabla J(\mathbf{p}) \propto \sum_s \mu(s) \sum_a \nabla\pi(a|s)q_\pi(s, a). \quad (\text{B8})$$

[1] E. Zermelo, *Z. Angew. Math. Mech.* **11**, 114 (1931).

[2] B. J. Nelson, I. K. Kaliakatsos, and J. J. Abbott, *Annual review of biomedical engineering* **12**, 55 (2010).

[3] B.-W. Park, J. Zhuang, O. Yasa, and M. Sitti, *ACS nano* **11**, 8910 (2017).

[4] M. T. Manzari, Y. Shamay, H. Kiguchi, N. Rosen,

- M. Scaltriti, and D. A. Heller, *Nature Reviews Materials* **6**, 351 (2021).
- [5] M. Trincavelli, M. Reggente, S. Coradeschi, A. Loutfi, H. Ishida, and A. J. Lilienthal, in *2008 IEEE/RSJ International Conference on Intelligent Robots and Systems (IEEE, 2008)* pp. 2210–2215.
- [6] P. F. Lermusiaux, D. Subramani, J. Lin, C. Kulkarni, A. Gupta, A. Dutt, T. Lolla, P. Haley Jr, W. H. Ali, C. Mirabito, *et al.*, *Journal of Marine Research* **75**, 765–813 (2017).
- [7] M. G. Bellemare, S. Candido, P. S. Castro, J. Gong, M. C. Machado, S. Moitra, S. S. Ponda, and Z. Wang, *Nature* **588**, 77 (2020).
- [8] F. Chai, K. S. Johnson, H. Claustre, X. Xing, Y. Wang, E. Boss, S. Riser, K. Fennel, O. Schofield, and A. Sutton, *Nature Reviews Earth & Environment* **1**, 315 (2020).
- [9] A. E. Bryson and H. Yu-Chi, *Applied Optimal Control: Optimization, Estimation, and Control* (Routledge, 2018).
- [10] L. Techy, *Intelligent Service Robotics* **4**, 271 (2011).
- [11] D. E. Kirk, *Optimal Control Theory: An Introduction* (Courier Corporation, 2004).
- [12] V. Angelo, C. Fabio, and C. Massimo, *Chaos: from simple models to complex systems* (World Scientific Publishing Company, 2009).
- [13] L. Biferale, F. Bonaccorso, M. Buzzicotti, P. Clark Di Leoni, and K. Gustavsson, *Chaos: An Interdisciplinary Journal of Nonlinear Science* **29** (2019).
- [14] G. K. Vallis, *Atmospheric and Oceanic Fluid Dynamics* (Cambridge University Press, 2017).
- [15] G. Boffetta and R. E. Ecke, *Annual Review of Fluid Mechanics* **44**, 427 (2012).
- [16] L. Piro, B. Mahault, and R. Golestanian, *New Journal of Physics* **24**, 093037 (2022).
- [17] R. Monthiller, A. Loisy, M. A. Koehl, B. Favier, and C. Eloy, *Physical Review Letters* **129**, 064502 (2022).
- [18] C. Calascibetta, L. Biferale, F. Borra, A. Celani, and M. Cencini, *Communications Physics* **6**, 256 (2023).
- [19] B. Yoo and J. Kim, *Journal of Marine Science and Technology* **21**, 334 (2016).
- [20] S. Colabrese, K. Gustavsson, A. Celani, and L. Biferale, *Physical Review Letters* **118**, 158004 (2017).
- [21] K. Gustavsson, L. Biferale, A. Celani, and S. Colabrese, *The European Physical Journal E* **40**, 110 (2017).
- [22] E. Schneider and H. Stark, *Europhysics Letters* **127**, 64003 (2019).
- [23] M. Buzzicotti, L. Biferale, F. Bonaccorso, P. Clark di Leoni, and K. Gustavsson, in *International Conference of the Italian Association for Artificial Intelligence* (Springer, 2020) pp. 223–234.
- [24] J. K. Alageshan, A. K. Verma, J. Bec, and R. Pandit, *Physical Review E* **101**, 043110 (2020).
- [25] P. Gunnarson, I. Mandralis, G. Novati, P. Koumoutsakos, and J. O. Dabiri, *Nature Communications* **12**, 7143 (2021).
- [26] M. Nasiri, H. Löwen, and B. Liebchen, *Europhysics Letters* **142**, 17001 (2023).
- [27] R. S. Sutton and A. G. Barto, *Reinforcement Learning: An Introduction*, 2nd ed. (The MIT Press, 2018).
- [28] <https://github.com/parfenyev/opt-navig/>.
- [29] H.-D. Ebbinghaus, *Ernst Zermelo: An approach to his life and work* (Springer, 2007).
- [30] S. V. Filatov, V. M. Parfenyev, S. S. Vergeles, M. Y. Brazhnikov, A. A. Levchenko, and V. V. Lebedev, *Physical Review Letters* **116**, 054501 (2016).
- [31] S. V. Filatov, S. A. Aliev, A. A. Levchenko, and D. A. Khramov, *JETP Letters* **104**, 702 (2016).
- [32] N. Francois, H. Xia, H. Punzmann, P. W. Fontana, and M. Shats, *Nature Communications* **8**, 1 (2017).
- [33] H. Xia, N. Francois, J.-B. Gorce, H. Punzmann, and M. Shats, *Fluids* **4**, 74 (2019).
- [34] V. Parfenyev, S. Filatov, M. Y. Brazhnikov, S. Vergeles, and A. Levchenko, *Physical Review Fluids* **4**, 114701 (2019).
- [35] A. P. Abella and M. N. Soriano, *Physica Scripta* **95**, 085007 (2020).
- [36] N. C. Constantinou, G. L. Wagner, L. Siegelman, B. C. Pearson, and A. Palóczy, *Journal of Open Source Software* **6**, 3053 (2021).
- [37] V. Valadão, G. Boffetta, F. De Lillo, S. Musacchio, and M. Cialesi-Esposito, *Journal of Turbulence*, 1 (2025).
- [38] A. Von Kameke, F. Huhn, G. Fernández-García, A. P. Munuzuri, and V. Pérez-Muñuzuri, *Physical Review Letters* **107**, 074502 (2011).
- [39] N. Francois, H. Xia, H. Punzmann, and M. Shats, *Physical Review Letters* **110**, 194501 (2013).
- [40] N. Francois, H. Xia, H. Punzmann, S. Ramsden, and M. Shats, *Physical Review X* **4**, 021021 (2014).
- [41] R. Colombi, M. Schlüter, and A. von Kameke, *Experiments in Fluids* **62**, 1 (2021).
- [42] R. Colombi, N. Rohde, M. Schlüter, and A. von Kameke, *Fluids* **7**, 148 (2022).
- [43] J. Sommeria, *Journal of Fluid Mechanics* **170**, 139 (1986).
- [44] J. Paret and P. Tabeling, *Physics of Fluids* **10**, 3126 (1998).
- [45] H. Xia, M. Shats, and G. Falkovich, *Physics of Fluids* **21**, 125101 (2009).
- [46] L. Bardóczy, A. Bencze, M. Berta, and L. Schmitz, *Physical Review E* **90**, 063103 (2014).
- [47] A. V. Orlov, M. Y. Brazhnikov, and A. A. Levchenko, *JETP Letters* **107**, 157 (2018).
- [48] H.-Y. Zhu, J.-H. Xie, and K.-Q. Xia, *Journal of Fluid Mechanics* **996**, A39 (2024).
- [49] D. P. Kingma and J. Ba, *arXiv preprint arXiv:1412.6980* (2014).
- [50] J. Nocedal and S. J. Wright, *Numerical optimization* (Springer, 2006).
- [51] A. G. Baydin, B. A. Pearlmutter, A. A. Radul, and J. M. Siskind, *Journal of Machine Learning Research* **18**, 1 (2018).
- [52] R. J. Williams, *Machine learning* **8**, 229 (1992).
- [53] T. Tieleman and G. Hinton, *COURSERA: Neural networks for machine learning* **4**, 26 (2012).
- [54] J. Duchi, E. Hazan, and Y. Singer, *Journal of Machine Learning Research* **12** (2011).
- [55] P. Mehta, M. Bukov, C.-H. Wang, A. G. Day, C. Richardson, C. K. Fisher, and D. J. Schwab, *Physics reports* **810**, 1 (2019).